Research Activities

– Synchrotron Radiation Experiments –

22AG027 BL-1

Interplay of Exchange and Spin-Orbit Interaction for Interface States in Ni/W(110)

Markus Donath[a], Pascal Jona Grenz[a] , Marcel Holtmann[a]
Shiv Kumar[b], Koji Miyamoto[b] and Taichi Okuda[b], and Kenya Shimada[b]

[a]Physikalisches Institut, University of Münster, Wilhelm-Klemm-Straße 10,
48149 Münster, Germany
[b]Hiroshima Synchrotron Radiation Center, Hiroshima University

Keywords: Nickel, tungsten, spin-orbit coupling, superstructure, exchange interaction, interface states

Due to the high atomic number of tungsten and the ferromagnetic behavior of Nickel, Ni/W(110) is a well-suited system for studying the interplay of spin-orbit coupling and exchange interaction. Furthermore, ultrathin Ni films on W(110) in the few-monolayer regime reveal a complex (7x1) superstructure and thus provide the possibility to study the influence of this superstructure on electronic bands.

Figure 1 (a)-(d) display constant energy cuts for 1ML Ni/W(110)-(7x1) for E- E_F = 0meV to −400meV. Various additional bands are visible compared with the clean W(110) surface. The observed band structure deviates significantly from the one of pristine W(110), and also, no congruence to a Ni(111) constant energy cut is apparent which suggests that many of the observed bands are induced by the interface.
To investigate the influence of the superstructure along the "7 direction", a measurement along the k_y-direction for k_x=1.25 $\mathrm{\AA}^{-1}$ (purple line in Fig. 1 (e), parallel to ΓH) is displayed in Fig. 1 (h). Two oval-shaped features are visible in Fig. 1 (e), marked by the black arrows. The $E(\mathbf{k}_\parallel)$ cut along the purple line reveals that the two ovals stem from states with linear dispersion. Besides the replication of these states, the linear dispersion over a large range of about 500meV is remarkable and strongly reminiscent of the Dirac-type surface state DSS described, e.g., in [1].

To evaluate the correlation of the (7×1) superstructure and the three pairs of bands $\epsilon_{1,2}$, $\epsilon_{3,4}$, and $\epsilon_{5,6}$, a comparison of the measurements for 0.5ML and 1ML Ni/W(110) along ΓH in the same $E(\mathbf{k}_\parallel)$ region is presented in Fig. 2. For a coverage of 0.5 ML, the Ni adlayer is pseudomorphic to the W(110) structure, i.e., no superstructure occurs. In 2 (a), only the $\epsilon_{1,2}$ bands are visible. This leads to the assumption that the occurrence of the three pairs of ϵ bands for the (7×1) structure is related to the additional periodic potential created by the superstructure. So far, only the occurrence of replica bands shifted by $\mathbf{G}_{(7\times1)}$ has been considered as a consequence of the superstructure. But, additionally, these bands should appear as mirrored bands starting at each $\Gamma_{(7\times1)}$ point. These mirrored bands are often low in intensity and not visible in ARPES experiments. These bands are therefore called ghost bands [2]**.** Nonetheless, these bands can be observed indirectly. If these ghost bands cross visible bands, hybridization gaps may be observed. At first glance, no gaps are visible in the ϵ bands, neither for the (1×1) nor the (7×1) structure in Fig. 2 (a) and (b), respectively. By analyzing the EDCs for various k_y in Fig. 2 (c) and (d), however, gaps within the ϵ_2 band for the (7×1) structure become apparent. In Fig. 2 (c), the EDCs show the two peaks of the ϵ_1 and ϵ_2 bands. In all of the EDCs, each band shows only one peak; thus, no gaps are observed for the (1×1) structure. For the (7×1) structure, the situation is different. The EDCs for k_y=0.54 $\mathrm{\AA}^{-1}$ to k_y=0.60 $\mathrm{\AA}^{-1}$ show again the two peaks for the ϵ_1 and the ϵ_2 band. The EDC for k_y=0.63 $\mathrm{\AA}^{-1}$, however, reveals a distinctly different behavior of the ϵ_2 band. Two peaks (indicated by black arrows) are present, separated by ≈ 200meV, instead of one ϵ_2 peak. For k_y = 0.66 $\mathrm{\AA}^{-1}$, the ϵ_2 band is again apparent by a prominent peak close to E_F. The splitting of the peak into two separate peaks in the EDC for k_y = 0.63 $\mathrm{\AA}^{-1}$ strongly indicates the formation of a gap.

Additional constant-energy-cut measurements for 3ML and 13ML of Ni on W(110) were conducted. The data reveal bands very similar to the results for a pristine Ni(111) surface. Visible are the exchange-split *sp*-bands as well as the majority-spin *d* bands of Ni. Further spin-resolved measurements are necessary to reveal the influence of SOI on the exchange-split Ni bands.

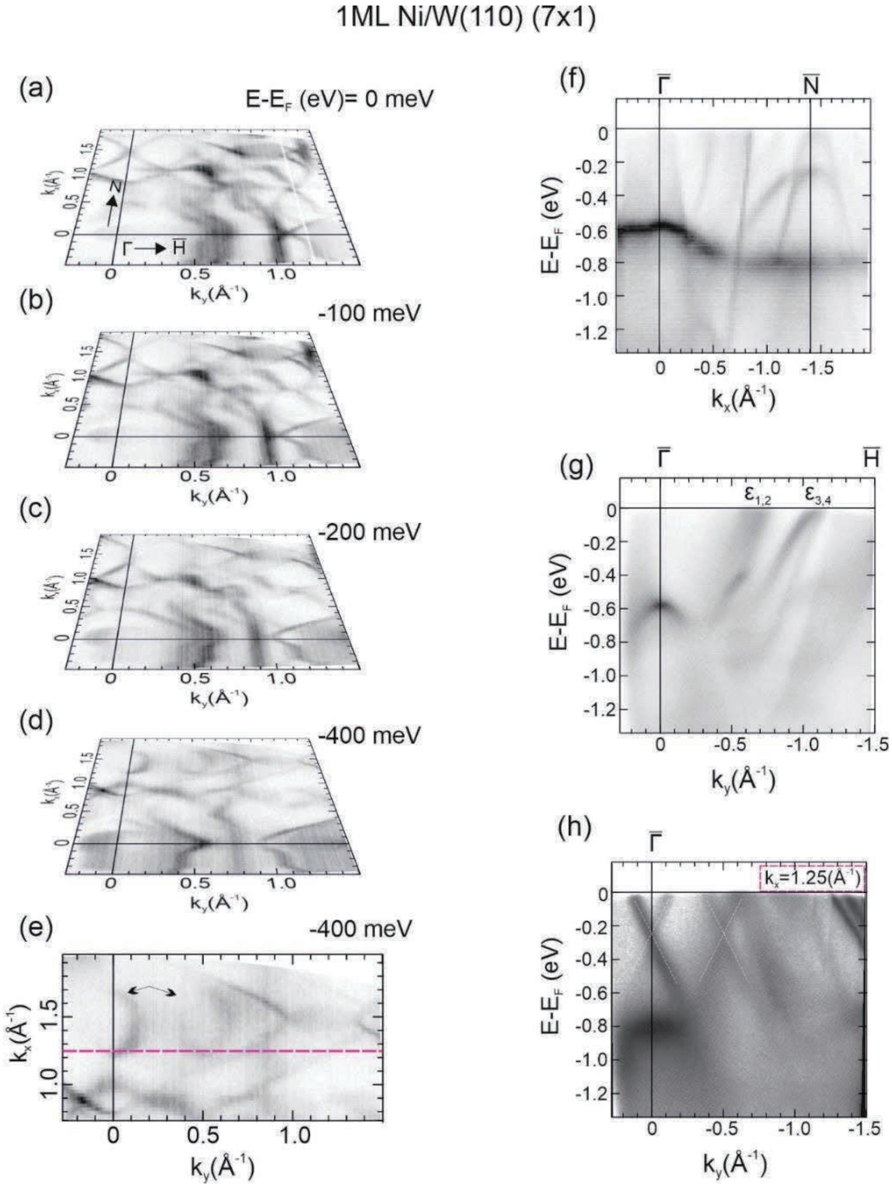

FIGURE 1. ARPES measurements of the occupied band structure of 1ML Ni/W(110)-(7×1). (a)-(d) show constant energy cuts at different binding energies, (e) shows an extract of the constant energy cuts displayed in (d). The purple line indicates the k_y-line for the $E(k_y)$ plot displayed in (h). (f) displays the $E(k_x)$ plot along the high-symmetry direction ΓN. (g) displays the $E(k_y)$ plot along the high symmetry direction ΓH. (h) displays the $E(k_y)$ plot for k_x=1.25 Å^{-1}. The white-dotted lines are guides to the eye for the two linearly dispersing states. For (h), a logarithmic scale was chosen to enhance the visibility of the linearly dispersing states. All plots are presented on a grayscale, where white represents low intensity and black high intensity.

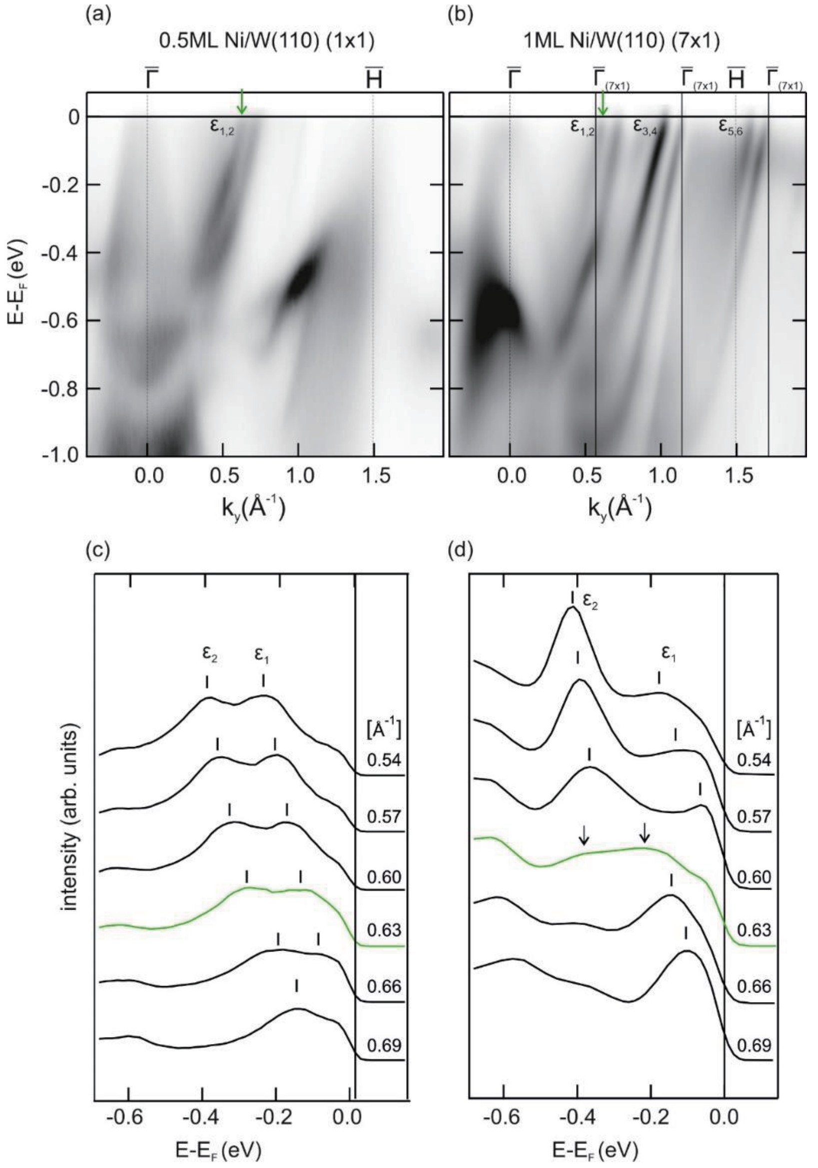

FIGURE 2. Displayed are $E(k_y)$ plots for (a) 0.5 ML and (b) 1ML Ni/W(110) measured along the high-symmetry line ΓH. The black-dotted lines indicate the high-symmetry points of the pristine W(110)-(1×1) surface. The black solid lines represent the Γ points of the (7×1) superstructure. The green arrows indicate k_y=0.63 Å^{-1}, the position of the green EDCs shown in (c) and (d). EDCs for various k_y values for 0.5 ML and 1ML Ni/W(110) are shown in (c) and (d), respectively. Black tick marks indicate the peak positions of ϵ_1 and ϵ_2. The black arrows in (d) indicate two peak positions.

REFERENCES

1. K. Miyamoto, A. Kimura, K. Kuroda, T. Okuda, K. Shimada, H. Namatame, M. Taniguchi, and M. Donath, *Phys. Rev. Lett.* **108**, 066808 (2012).
2. M. Thaler, D. Steiner, A. Menzel, F. Mittendorf, and E. Bertel, *Phys. Rev. Res.* **2**, 043156 (2020).

22AG036 BL-1

Study of Fermi Surface Topology on CoP-Based ThCr$_2$Si$_2$ Structural Compounds *A*Co$_2$P$_2$ (*A* = Ca, Sr, La, Ce, Pr, Nd, Eu)

Xiaoming[a] and Chang Liu[a]

[a] *Department of Physics and Shenzhen Institute for Quantum Science and Engineering (SIQSE), Southern University of Science and Technology (SUSTech), Shenzhen, Guangdong 518055, China*

Keywords: CoP based ThCr$_2$Si$_2$ Structure, Fermi Surface Topology, Angle Resolved Photoemission Spectroscopy

The ThCr$_2$Si$_2$ structure is a classic quasi-2D tetragonal system with the crystal group of I4/mmm. Early research work mainly focused on exploitation of new compounds and their magnetic properties [1-7]. So far, more than a thousand materials with the ThCr$_2$Si$_2$ structure have been discovered. The richness of materials has provided a fertile platform for the research of novel physics. Prominent examples include CeCu$_2$Si$_2$, the first unconventional superconductor, URu$_2$Si$_2$, the famous hidden-order superconductor, and YbRh$_2$Si$_2$, a prototypical material to explore quantum criticality [7]. And of course, the most famous ones are *A*Fe$_2$As$_2$ (*A* = Ca, Sr or Ba), parent compounds of the "122"-family of iron-based high-T_C superconductors [8-10]. The ground states of the *A*Fe$_2$As$_2$ compounds exhibit antiferromagnetic (AFM) spin density wave (SDW), which has attracted enormous attention for its intimate connection with superconductivity (SC). Therefore, the investigation of how the band structure and Fermi surface topology are related to the magnetic ordering and even SC has aroused great interest [8-14]. In this report, we focused on the analogical CoP-based ThCr$_2$Si$_2$ structural compounds, *A*Co$_2$P$_2$ (*A* = Ca, Sr, La, Ce, Pr, Nd, Eu). Different from the iron pnictides that host similar AFM ground state magnetic order, *A*Co$_2$P$_2$ exhibit rich magnetic structures at low temperatures, which are highly dependent on the *A*-site cation. As shown in Fig. 1(a), SrCo$_2$P$_2$ does not have long range magnetic order, for EuCo$_2$P$_2$, only Eu atoms carry magnetic moment in a complicated incommensurate SDW form, whereas magnetic orders due to cobalt moments was observed in CaCo$_2$P$_2$, CeCo$_2$P$_2$, LaCo$_2$P$_2$, PrCo$_2$P$_2$ and NdCo$_2$P$_2$ [2-6]. The diversity of the magnetic structure implies that the CoP based *A*Co$_2$P$_2$ compounds are a good platform for studying the intimate connection between the magnetic structure and the Fermi surface topology. Therefore, we plan to carry out systematic Fermi surface topology studies on the *A*Co$_2$P$_2$ systems.

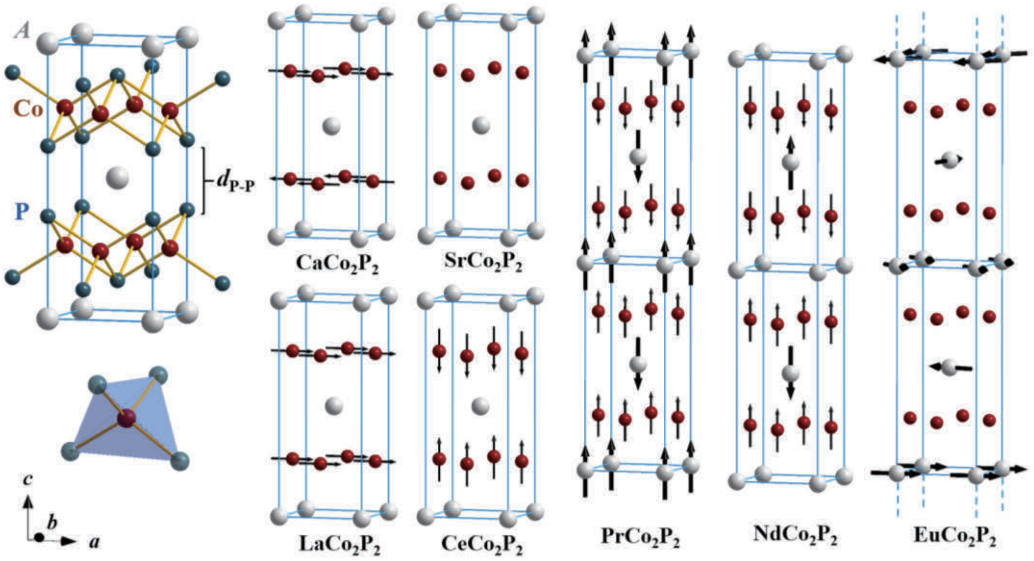

FIGURE 1. Magnetic structures of *A*Co$_2$P$_2$. The cobalt atoms (red circles) with their ordered magnetic moments are shown together with the *A* atoms (grey circles), which are in the positions (0 0 0) and (1/2 1/2 1/2) of the unit cell. [6]

We employed the high resolution angle resolved photoemission spectroscopy (ARPES) setup at BL-01 of HiSOR to investigate the electronic band structure of $CaCo_2P_2$. Like most compounds with $ThCr_2Si_2$ structure, $CaCo_2P_2$ single crystals can be easily cleaved along the [00*l*] direction. All the samples are cleaved and measured *in-suit* at 20 K, which is below the Neel temperature of 100 K. Through a k_z map with photon energies from 100 to 200 eV, we were able to determine the inner potential to be 13 eV. After that, we set the photon energy to 128 eV ($k_z \approx 18\ \pi/c$) to conduct the high-quality Fermi surface maps and band structure measurements along high symmetry directions. As shown in Fig. 2(a)-(d), the bands show rectangle symmetry, consistent with the symmetry of the (00*l*) surface of the $CaCo_2P_2$. As shown in the four *k-E* cuts provided in Fig. 2(e)-(h), a Dirac-like band is observed at the *Z* point. Further analysis requires support from first principles calculations.

In summary, we have systematically measured the electronic band structure of $CaCo_2P_2$ in the AFM state. In the future, we plan to conduct detailed, temperature-dependent measurements of ACo_2P_2 systems with other *A* site cations.

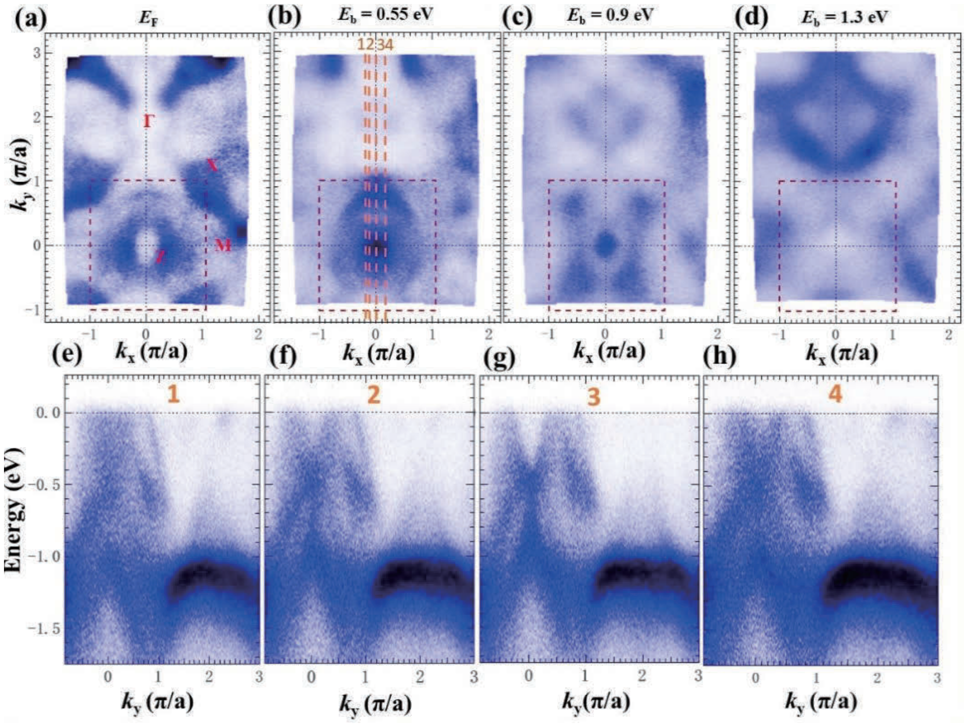

FIGURE 2. ARPES results of $CaCo_2P_2$. (a)–(d) the ARPES constant-energy contour at E_B = 0, 0.55, 0.9 and 1.3 eV with $h\nu$ = 128 eV. (e)-(h) *E*- *k* cuts at positions marked by dash lines on (b).

REFERENCES

1. R. Marchand and W. Jeitschko, Ternary Lanthanoid-Transition Metal Pinictides with $ThCr_2Si_2$-Type Structure. J. Solid State Chem. **24**, 351 (1978).
2. M. Reehuis and W. Jeitschko, Structure and Magnetic Properties of the Phosphides $CaCo_2P_2$ and LnT_2P_2 with $ThCr_2Si_2$ Structure and *LnT*P with PbFCl Structure (*Ln* = Lanthanides, *T* = Fe, Co, Ni), J. Phys. Chem. Solids **51**, 961 (1990).
3. M. Reehuis et al., A Neutron Diffraction Study of the Magnetic Structure of $EuCo_2P_2$, J. Phys. Chem. Solids **53**, 687 (1992).
4. M. Reehuis et al., A Neutron Diffraction Study of the Magnetic Order in the $ThCr_2Si_2$ Type Phosphides $PrCo_2P_2$ and $NdCo_2P_2$, J. Phys. Chem. Solids **54**, 469 (1993).
5. M. Reehuis et al., Ferromagnetism in the $ThCr_2Si_2$ Type Phosphide $LaCo_2P_2$, J. Magn. Magn. Mater. **138**, 85 (1994).
6. M. Reehuis et al., Antiferromagnetic Order in the $ThCr_2Si_2$ Type Phosphides $CaCo_2P_2$ and $CeCo_2P_2$, J. Alloy. Compd. **226**, 54 (1998).
7. K. Kliemt et al., Crystal Growth of Materials with the $ThCr_2Si_2$ Structure Type, Cryst. Res. Technol. **55**, 1900116 (2020).
8. Y. Kamihara et al., Iron-Based Layered Superconductor $La[O_{1-x}F_x]FeAs$ (x = 0.05−0.12) with T_c = 26 K, J. Am. Chem. Soc. **130**, 3296 (2008)
9. M. Rotter et al., Spin-Density-Wave Anomaly at 140 K in the Ternary Iron arsenide $BaFe_2As_2$, Phys. Rev. B **78**, 020503 (R) 2008.

10. M. Yi et al., Electronic Structure of the $BaFe_2As_2$ Family of Iron-Pnictide Superconductors, Phys. Rev. B **80**, 024515 2008.
11. F. Rullier-Albenque et al., Hole and Electron contributions to the transport properties of $Ba(Fe_{1-x}Ru_x)_2As_2$ Single Crystals, Phys. Rev. B **81**, 224503 (2010).
12. G. Liu et al., Band-structure reorganization across the magnetic transition in $BaFe_2As_2$ seen via high-resolution angle-resolved photoemission, Phys. Rev. B **80**, 134519 (2008)
13. B. Saparov et al., Complex Structures of Different $CaFe_2As_2$ Samples, Sci. Rep.-UK **4**, 4120 (2014)
14. Q. Guo et al., Superconductivity at 3.85 K in $BaPd_2As_2$ with the $ThCr_2Si_2$-Type Structure, EPL **113**, 17002 (2016).

22BG004, 23BU010 BL-1, IPES

Research of Charge Fluctuations in the Electron-doped High-T_c Cuprate NCCO Revealed by ARPES and IPES

H. Yamaguchi[a], Y. Onishi[b], Y. Miyai[b], Y. Tsubota[b], M. Atira[c], K. Tanaka[d],
H. Sato[c], D. Song[e], K. Shimada[b,c], S. Ideta[b,c]

[a] School of Science, Hiroshima Univ., Higashi-Hiroshima 739-0046, Japan
[b] Graduate School of Advanced Science and Engineering, Hiroshima Univ., Higashi-Hiroshima 739-0046, Japan
[c] Hiroshima Synchrotron Radiation Center (HiSOR), Hiroshima Univ., Higashi-Hiroshima 739-0046, Japan
[d]UVSOR-Ⅲ Synchrotron, Institute for Molecular Science., Okazaki, Aichi 444-8585, Japan
[e] Stewart Blusson Quantum Matter Institute,University of British Columbia,Vancouver, BCV 6T1Z4,Canada

Keywords: cuprate superconductors, charge fluctuation, electronic structure, ARPES, IPES

The origin of the high-Tc superconductivity has been extensively studied so far, but the bosonic interaction to form electron pairs is still elusive. There are three degrees of freedom in the solid; orbital, charge, and spin [1]. According to the previous experimental reports [2-8], the promising candidates of the bosonic interactions are phonons and magnons. On the other hand, the role of the charge fluctuation in the high-Tc superconductivity is not well understood.

Recently, inelastic X-ray scattering experiments reported that charge excitations for both hole- and electron-doped cuprate high-T_c superconductors [9-11], and therefore, the effect of the charge fluctuation to the high-T_c superconductivity has attracted interest. According to the theoretical study [12], using the layered *t*-*J* model, the electron self-energy is calculated and discussed about the effect of charge fluctuation in the spectral function.

We have performed an ARPES and inverse photoemission spectroscopy (IPES) to observe the electronic structure in the occupied and unoccupied states, respectively, on $Nd_{1-x}Ca_xCuO_4$ ($x = 0.15$) as shown in Fig. 1. We find that a strong peak structure exists in the energy region between 5 and 9 eV above the Fermi level (E_F). In the poster presentation, we will show the details about the experimental data and discuss the effect from the charge fluctuation.

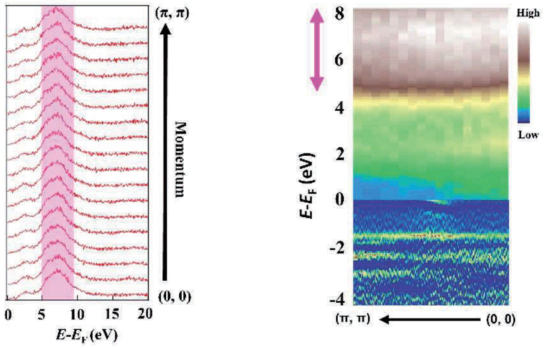

FIGURE 1. Experimental data observed by ARPES and IPES. Energy-distribution curves observed by IPES in the direction of (0, 0)-(π, π) is shown on the left side. On the right side, IPES spectra without the second derivative (above E_F) and the second-derivative intensity plot observed by ARPES (below E_F) is shown.

REFERENCES

1. H. Hwang *et al.*, Nat. Mater. **11**, 103-113 (2012).
2. A. Lanzara *et al.*, Nature **412**, 510 (2001).
3. J. P. Carbotte *et al.*, Nature **401**, 354 (1999).
4. H. F. Fong *et al.*, Phys. Rev. Lett. **75**, 316 (1995).
5. L. Braicovich *et al.*, PhysRevLett. **104**, 077002 (2010).
6. M. Le Tacon *et al.*, Nature Phys **7**, 725-730 (2011).
7. J. Schlappa *et al.*, Nature **485**, 82-85 (2012).
8. M. P. M. Dean *et al.*, Nature materials **12**,1019-1023 (2013).
9. J. Lin *et al.*, npj Quantum Mater. **5**, 4 (2020).
10. A. Singh *et al.*, Phys. Rev. B **105**, 235105 (2022).
11. W. S. Lee *et al.*, Nature Phys **10**, 883-889 (2014).
12. H. Yamase *et al.*, Phys. Rev. B, **104**, 045141 (2021).

Uncovering Nonsymmorphic Symmetry Protected Hidden Spin Polarization in Inversion-symmetric Multiphase Superconductor Ce(RhAs)$_2$

Ke Zhang[a], Yesen Feng[a], Yudai Miyai[b], Yogendra Kumar[b], Shin-ichiro Ideta[b],
Kenya Shimada[b] and Liang Qiao[a]

[a] School of Physics, University of Electronic Science and Technology of China, Chengdu 610054, China
[b] *Research Institute for Synchrotron Radiation Science, Hiroshima University, Higashi-Hiroshima 739-0046, Japan*

Keywords: Nonsymmorphic Symmetry, Hidden Spin Polarization, Multiphase Superconductor, Inversion-symmetric.

A combination of both time-reversal and space inversion symmetries yields spin-degenerated energy levels in solids. A relativistic electron moving in an electric field experiences an effective magnetic field that interact on an electron spin, giving rise to the spin-orbit coupling (SOC). The spin splitting induced by the SOC can be classified into the Dresselhaus type and Rashba type [1-3]. However, giant Rashba-type spin splitting has been found experimentally in centrosymmetric crystals such as BiOI [3] and GeTe [4]. These spin-polarization effects originate from specific atomic sites with point group asymmetries, rather than, as generally accepted, from the asymmetry of the global crystal space group. The local gradient of the electric potential, protected by the local crystal asymmetries, appears in the spin-orbit Hamiltonian, such that even in centrosymmetric systems this electric field does not have to vanish at all atomic sites. The spin textures are located at different sectors, which is called hidden spin polarization (HSP).

Recently, there has been an upsurge of interest in materials in which both spin-orbit coupling and strong correlations are important. The heavy fermion material $CeRh_2As_2$ is a variant of non-centrosymmetric heavy fermion superconductor [5]. The crystal structure is globally centrosymmetric (with well-defined inversion centers) but is locally non-centrosymmetric, with an inversion symmetry linking two non-centrosymmetric Ce-square lattices. This configuration can be compared with the relation between ferromagnetic (FM) and antiferromagnetic (AF) structures. The FM state globally breaks time-reversal symmetry; the AF state does not but has two sublattices of subunits violating time-reversal symmetry. The consequence of such a structure in $CeRh_2As_2$ is that even-parity (spin-singlet) and odd-parity (spin-triplet) Cooper pairs are not mixed, so that a phase transition between even- and odd-parity condensates should occur inside the superconducting condensate [6].

Spin- and angle-resolved photoemission spectroscopy (SARPES) has been instrumental in studying the consequences of such interplay for the electronic structure of a variety of materials. However, because of earlier predictions of negligible spin-orbit interaction in cuprates, the full spin character of quasiparticles has not been probed experimentally. Here, we report such a study, revealing unexpected HSP effect of the spin-orbit interaction for the multiphase heavy fermion superconductor $CeRh_2As_2$.

The $CeRh_2As_2$ is quasi 2D materials which contains two opposites sectors for per unit cell, while the global crystal symmetry is centrosymmetric, each sector contacts by nonsymmorphic symmetry with glide mirror reflection and screw axis operation forming a buckling structure. The spin polarization is thus well protected by nonsymmorphic symmetry contact of each sector: the spin-up and spin-down electrons are ideally separated without compensation in each sector even the opposite sectors are close to each other. As a result, the crystal potentials or dipole fields superpose together, leading to effective magnetic fields to create peculiar spin textures projected to each sector: Rashba spin texture with helical structure around X point and Dresselhaus spin texture without helical structure around M point.

By checking the Fermi surface, we first located the high symmetric directions in the BZ. Figure 1 shows the Fermi surface of the $CeRh_2As_2$ sample. Figure 2 shows the high symmetric paths of X-G-X and M-X-M directions. Figure 1 displays the measured constant-energy plots within the kz = 0 plane at binding energy of $E_B = 0$ eV. One can directly identify one square like hole pocket centered at the Γ point and one nearly diamondlike electron pocket centered at the M point. These two pockets are further evidenced by the subsequent high-precision photoemission intensity [Fig. 2].

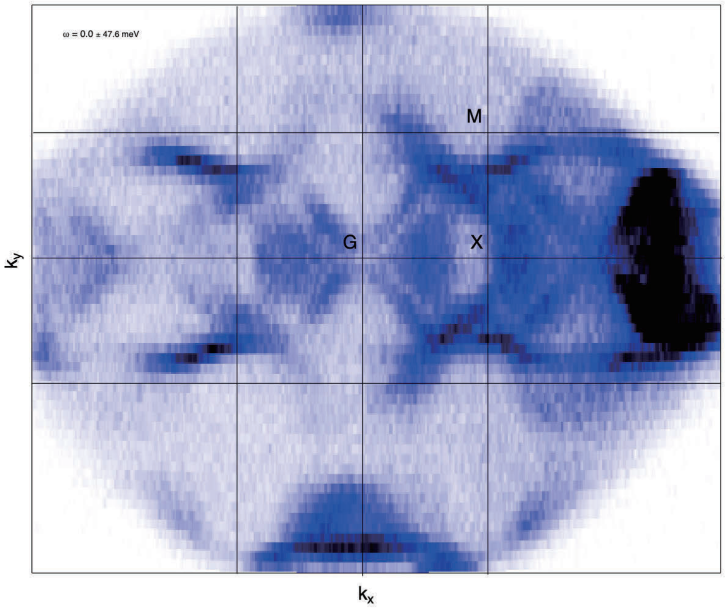

FIGURE 1. Fermi surface of $CeRh_2As_2$.

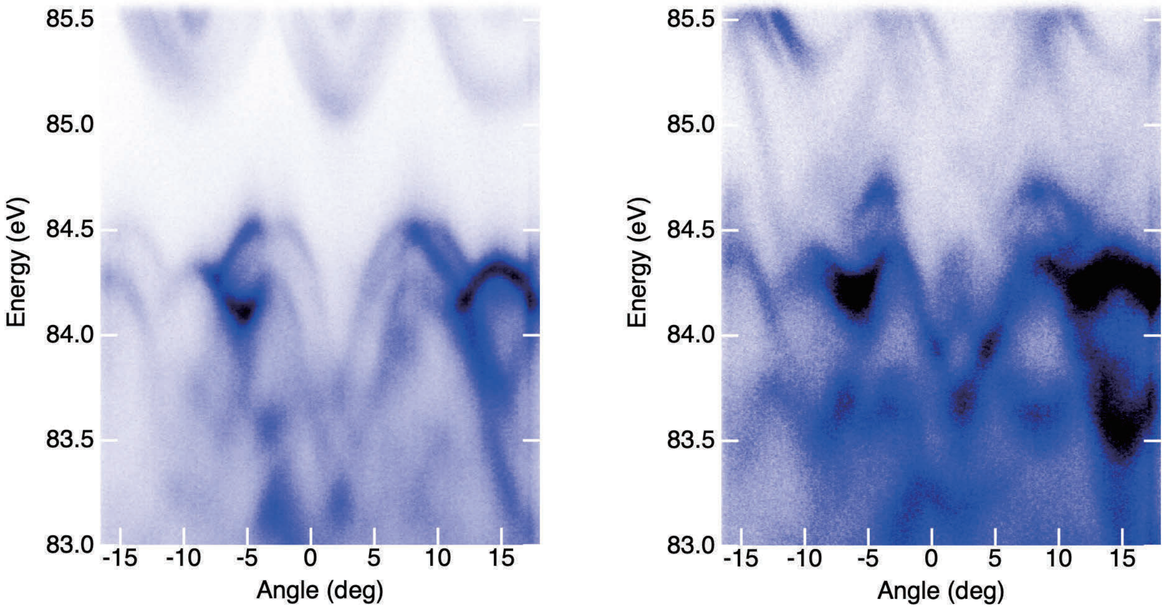

FIGURE 2. high symmetric paths of X-G-X and M-X-M directions.

REFERENCES

1. Zhang X, Liu Q, Luo J-W, et al., *Nature Physics* **10**, 387 (2014).
2. Yuan L, Liu Q, Zhang X, Luo J-W, *et al.*, *Nature Communications* **10**,906(2019).
3. K Zhang, S Zhao, Z Hao, *et al., Physical Review Letters* **127**, 126402 (2021).
4. Di Sante D, Barone P, Bertacco R, Picozzi S. *Advanced Materials* **25**, 509-513 (2013).
5. Gotlieb *et al., Science* **362**, 1271–1275 (2018).
6. S. Khim *et al., Science* **373**, 1012 (2021).

Observation of fully spin-polarized surface states in Bi2O2Se

Ke Zhang[a], Yesen Feng[a], Yudai Miyai[b], Yogendra Kumar[b], Shin-ichiro Ideta[b],
Kenya Shimada[b] and Liang Qiao[a]

[a] School of Physics, University of Electronic Science and Technology of China, Chengdu 610054, China
[b] *Research Institute for Synchrotron Radiation Science, Hiroshima University, Higashi-Hiroshima 739-0046, Japan*

Keywords: Bismuth oxyselenide, Hidden Spin Polarization, Semiconductor, Inversion-symmetric, surface state.

Owing to ultrahigh mobility (@1.9K, ~29000cm^{2}V^{-1}·s^{-1}; @room temperature, 450cm^{2}V^{-1}·s^{-1}) [1,2], outstanding air stability [3], moderate and tunable bandgap (~0.8eV and thickness dependent) [2,4], as well as the virtue of quick response to various input signals [5,6], Bi_2O_2Se is expected as an emerging material platform for the next-generation electronic industry [7–11]. Recently, diverse applications of Bi_2O_2Se are being extensively studied, including optoelectronic devices [12], field-effect transistors [2], memristors [6], photodetector [13,14], true random number generator and sensors [15–17]. Among them, massive efforts on combining 2D Bi_2O_2Se with other materials, such as graphene [18,19], transition metal dichalcogenides (TMDs) [20–23], topological materials [24] etc., have produced many sophisticated artificial heterojunctions with novel properties.

To realize the full potential of Bi_2O_2Se and explore its applications in electronic, thermoelectric, and optoelectronic devices, understanding its detailed electronic structures is essential. For this purpose, we performed angle-resolved photoemission spectroscopy (ARPES) measurement.

As shown in Figure 1, ARPES measurements were carried out on PLD-grown 1-UC (bilayer) Bi_2O_2Se films with photons of 98 eV. Figure 2 presents the general high-symmetry band dispersions along Γ–X and X–M, which is dominated by two hole-like bands α and β near VBM around X point. In the constant energy contours, the evolution of this two hole-like bands at higher binding energy is clearly observed. By magnifying the spectra around Γ near the Fermi level, we observe weak intensity from the bottom of the conduction band, indicating the existence of an indirect bandgap in Bi_2O_2Se. We do not observe any in-gap states such as the pinned impurity state throughout the whole 2D Brillouin zone, indicating high quality of MBE-grown 1-UC Bi_2O_2Se film.

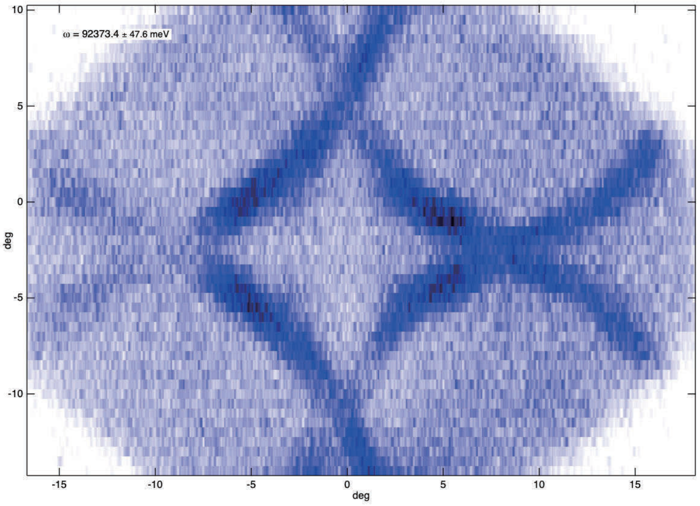

FIGURE 1. Fermi surface of the Bi_2O_2Se

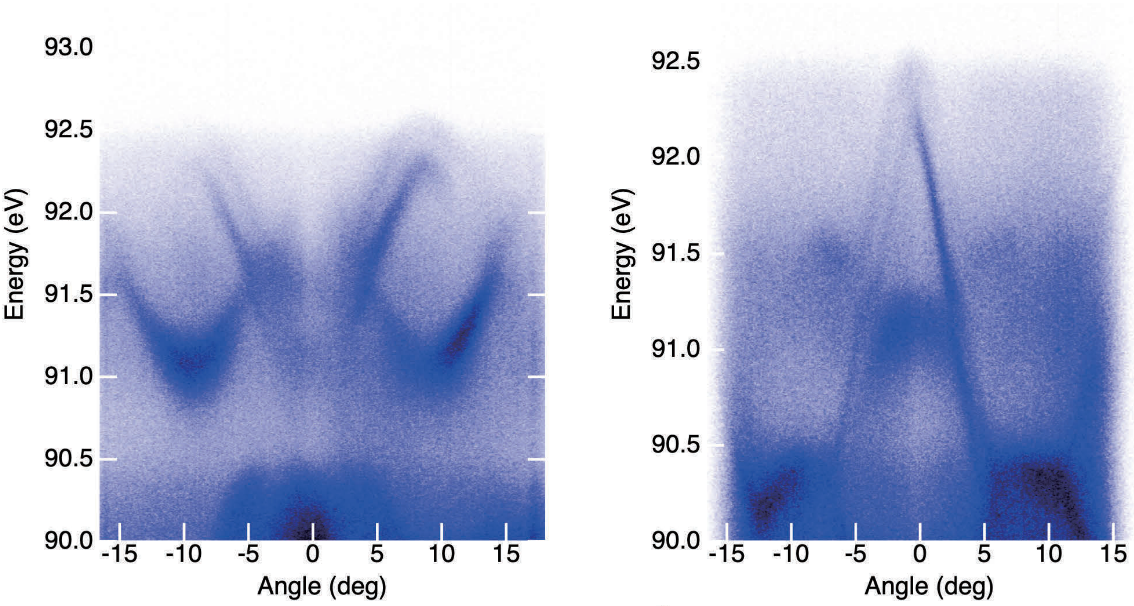

FIGURE 2. high symmetric paths of X-G-X and M-X-M directions.

REFERENCES

1. Zhu Z, et al. *J Am Chem Soc*. **144**(10):4541–4549 (2022).
2. Wu J, et al. *Nature Nanotech.* **12**:530–534 (2017).
3. Khan U, et al. *Small.* **19**:2206648 (2023).
4. Wu J, et al. *Nano Lett.* **17**(5):3021 (2017).
5. Luo P, et al. *Adv Funct Mater.* **31**(8):2008351(2021).
6. Dong Z, et al. *Nano Lett*. **23**(9):3842–50 (2023).
7. Sun Y, et al. Advanced Functional Materials. 2020;30(49):2004480.
8. Chen W, et al. Advanced Powder Materials. 2023;2(1):100080.
9. Meng JP, et al. Vacuum. 2017;145:268-71.
10. Li T, et al. Acc Mater Res. 2021;2(9):842–53.
11. Ding X, Matter. 2022;5:4274–314.
12. Wu J, et al. Adv Mater. 2017;29(44):1704060.
13. Chen Y, et al. Adv Funct Mater. 2021;31(14):2009554.
14. WU JH, et al. ACS Nano. 2021;15(10):15982-91.
15. Fu QD, et al. Adv Mater. 2019;31:1804945.
16. Liu B, et al. ACS Nano. 2022;16(4):6847–57.
17. Wang W, et al. Adv Mater. 2023;35:2210854.
18. Yang C, et al. Adv Funct Mater. 2020;30(30):2001598.
19. Hong C, et al. ACS Nano. 2020;14(12):16803–12.
20. Wang Z, et al. Adv Mater. 2021;33:2007503.
21. Tan C, et al. InfoMat. 2019;1(3):390–5.
22. Yang T, et al. J Mater Sci. 2019;54:14742–51.
23. Liu S, et al. Small. 2022;18(7):2106078.

The Electronic Structure of Pd Overlayers on Single Crystal $MoS_2(0001)$

Wai Kiat Chin,[a] Takashi Komesu,[a] Yogendra Kumar,[b] Amit Kumar,[b]
Yuudai Miyai,[b] Shin-ichiro Ideta,[c] Kenya Shimada,[c] and P. A. Dowben[a]

[a]*Department of Physics and Astronomy, Theodore Jorgensen Hall, 855 N 16th, University of Nebraska, 880299, Lincoln, NE 68588-0299, U.S.A.*
[b]*Graduate School of Science, Hiroshima University, Kagamiyama 1-3-1, Higashihiroshima 739-8526, Japan*
[c]*Hiroshima Synchrotron Radiation Center, Hiroshima University, 2-313 Kagamiyama, Higashihiroshima 739-0046, Japan*

Keywords: High Resolution Angle Resolved Photoemission Spectroscopy, Electronic Structure, MoS_2

Among the various metal contacts, to the metal dichalcogenides, palladium (Pd) has been seen to be a more efficient contact for hole injection into WSe_2 [1,2]. As MoS_2 is generally an n-type semiconductor (unlike WSe_2), we would expect that Pd would be a blocking contact. Previously we have been reported on $\bar{\Gamma}-\bar{K}$ band structure of Pd overlayer doping of the $MoS_2(0001)$ single crystal surface [3]. We saw a band shift of the $MoS_2(0001)$, with the deposition of low coverages of Pd, that tend to show more even n-type character of electronic structure for the valence band but also a general opening of the band gap of $MoS_2(0001)$ at the interface with Pd [3].

After preforming *in situ* cleaving of MoS_2 bulk crystals, the occupied valence electronic states of TMDs systems before and after Pd deposition were measured by high-resolution angle-resolved photoemission spectroscopy (HR-ARPES) at the linear undulator beamline (BL-1) at HiSOR, Hiroshima University in Japan, as detailed elsewhere [4]. All measurements were taken at a photon energy of $h\nu$ = 150 eV, with p-polarized light along the 2-dimensional (2D) direction (k_x and k_y in k-space) of the surface Brillouin zone (SBZ), at room temperature. Over-layers of Pd deposition were accomplished through use of an e-

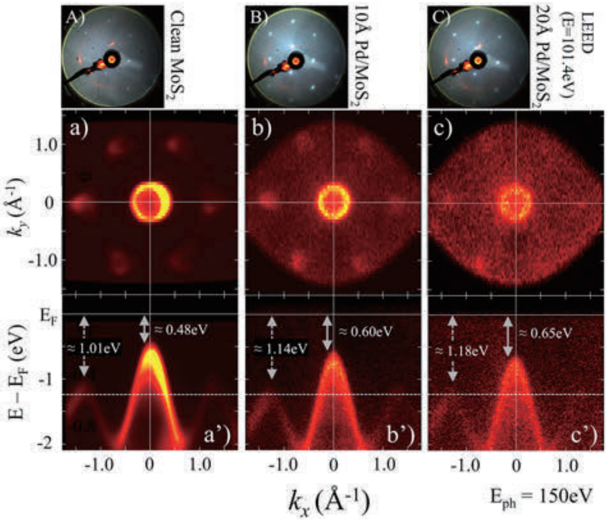

Figure 1. At the top, panels, A), B) and C), show the 3 pictures of the low energy electron diffraction (LEED) for clean MoS_2, 10 Å and 20 Å Pd deposited on on a $MoS_2(0001)$ respectively. This hexagonal diffraction pattern is characteristic of $MoS_2(0001)$. The figures, in center and bottom, are the result from the angle-resolve photoemission spectroscopy (taken at HiSOR) on clean $MoS_2(0001)$ single crystal, in a) and a'), and thin film overlayers of Pd on a $MoS_2(0001)$ single crystal, b) and b') for 10 Å, and c) and c') for 20 Å. The center panels, a), b), and c), are the slice of 2D mapping at the E = -1.25 eV below Fermi level (E_F), indicated in dashed line in a'), b') and c'), constructed from the band dispersion in k_y (top left) and k_x (bottom right), in k-space band structure mappings. The measurements were performed at room temperature. Those a'), b') and c') panels are the k_x direction of band dispersion at k_y = 0 line.

beam evaporator.

The low energy electron diffraction (LEED) of the Pd adlayer on the $MoS_2(0001)$ surface, as shown in Figure 1, A), B) and C), shows clear evidence of a well ordered $MoS_2(0001)$ surface, with the Pd(111) adlayer relative lattice matched with little disorder. The angle-resolve photoemission spectroscopy (ARPES) tells a different story. In Figure 1, a), b) and c), center panels, results of experimental electronic 2D band mapping are shown, for clean $MoS_2(0001)$ in a) and 10 Å in b) and 20 Å in c), Pd depositing on top of $MoS_2(0001)$ single crystal. The results also show an ordered Pd(111) adlayer on the $MoS_2(0001)$ surface, with apparent hexagonal patterns at SBZ edge, of the C_{3v} surface termination. This is superficially consistent with the LEED result, as seen on Figure 1, A), B) and C). In Figure 1, a') and b') and c'), the Pd shows that there is a shift of the entire valence band toward higher binding energy side, away from Fermi level (E_F), as reported previously [3] The increase in the background and changing intensity ratios of the band at $\overline{\Gamma}$ (center of SBZ) and $\overline{K}$ (edge of SBZ) do indicate that the $MoS_2(0001)$ band structure not only exhibits a rigid band shift but is increasing perturbed by the Pd adlayer. What is novel is that, in spite of the well-defined order, seen in LEED, the band structure acquires a background. These results point to strong hybridization at the Pd to MoS_2 (000) interface.

References

1. H. Fang, S. Chuang, T. C. Chang, K. Takei, T. Takahashi, A. Javey, *Nano Lett.* **12**, 3788–92 (2012)
2. S. Das, J. Appenzeller, *Appl. Phys. Lett.* **103**, 103501 (2013)
3. Prescott E Evans, Takashi Komesu, Eike F Schwier, Shiv Kumar, Kenya Shimada and Peter A Dowben, *J. Phys.: Condens. Matter* **32**, 465001 (2020)
4. K. Shimada, M. Arita, Y. Takeda, H. Fujino, K. Kobayashi, T. Narimura, H. Namatame and M. Taniguchi, *Surf. Rev. Lett.* **9** 529 (2002)

Modification Of The Electronic Structure Of Intrinsic Magnetic Topological Insulator $(Mn_{1-x}A_x)Bi_2Te_4$ By Substituting Mn With Non-Magnetic Elements Ge, Pb, Sn

D.A. Estyunin[a], T.P. Estyunina[a] and A.M. Shikin[a]

[a] *Saint Petersburg State University, 198504 Saint Petersburg, Russia*

Keywords: magnetic topological insulators, $MnBi_2Te_4$.

The introduction of a magnetic interaction into a topological insulator (TI) can lead to a number of quantum effects, such as the quantum anomalous Hall effect (QAHE), the topological magnetoelectric effect and, in the case of contact with a superconductor, the realization of Majorana fermions [1,2]. Currently, the most promising platform for studying the interaction between magnetism and topology is the intrinsic magnetic TI $MnBi_2Te_4$ [1-7]. However, for the efficient application of magnetic TIs in devices, it is necessary to be able to manipulate their electronic and magnetic properties in a controlled manner. For example, $MnBi_2Te_4$ is strongly n-doped and for the realization of QAHE it is necessary to shift the Dirac point to the Fermi level. This can be achieved by partial substitution of Bi atoms with Sb atoms. The electronic structure of the topological surface state (TSS) and the magnetic properties of the TI are preserved during such substitution.

Control of the magnetic properties is also desirable. In the ground state, $MnBi_2Te_4$ is in the antiferromagnetic state and the remagnetisation field is very high: about 7.5 T [3]. From a practical point of view, reducing this remagnetisation field will make it possible to create systems in which the transition from the axion insulator state to the Chern insulator state, as well as the change in the direction of the edge current in the QAHE state, can be achieved by applying much lower external magnetic fields. This field can be reduced by decreasing the magnetic interaction in the TI. This can be achieved by partial substitution of Mn atoms by non-magnetic elements (Sn, Pb, Ge) which are components of ternary TIs $SnBi_2Te_4$, $PbBi_2Te_4$, $GeBi_2Te_4$ with crystal structures similar to $MnBi_2Te_4$ [8-11].

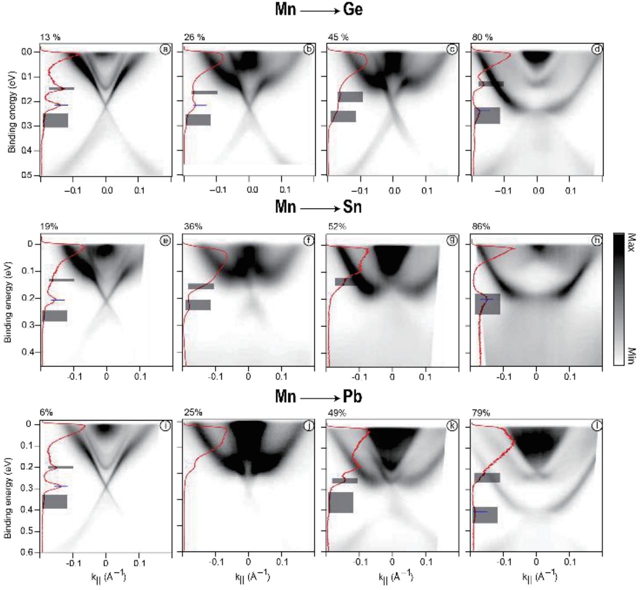

FIGURE 1. Dispersion relations for $Ge_xMn_{1-x}Bi_2Te_4$ (a-d), $Sn_xMn_{1-x}Bi_2Te_4$ (e-h), $Pb_xMn_{1-x}Bi_2Te_4$ (i-l) with different level of substitution (x) of Mn for the corresponding non-magnetic element. ARPES spectra were obtained using laser radiation with hv = 6.3 eV at temperature T = 15 - 30 K. Concentrations for these samples evaluated by EDX/XPS methods are shown on top of the panels. Profiles cut at the Γ-point are shown on the left side of the panels. Where possible, black rectangles mark the edges of the valence and conduction bands, blue line marks the position of the Dirac point of the TSS.

Moreover, the TIs (Ge,Sn,Pb)Bi_2Te_4 have a different full topological Z_2 invariant compared to $MnBi_2Te_4$, i.e. (1;111) and (1;000), respectively [9,11]. Therefore, at a certain substitution ratio of Mn for Ge, Sn, Pb in mixed crystals, a topological phase transition can be expected. In such crystals 3D Dirac/Weyl states can be realize.

Three sets of $(Mn_{1-x}A_x)Bi_2Te_4$ samples, with Mn substituted by A = (Ge, Sn, Pb), were investigated using angle-resolved photoelectron spectroscopy (ARPES) with laser photoexcitation (hν = 6.3 eV). The resulting dispersion relations are shown in Fig. 1. It is evident that for low levels of Mn substitution (x < 20%), the electronic structure of the mixed crystals remains similar to that of $MnBi_2Te_4$. The TSS is clearly visible, and its Dirac point can be clearly identified (marked by the blue horizontal line). The lower edge of the conduction band (CB) is sharp and well-defined. In panels (a) and (i), a splitting of the edge state into two sub-states is observed (see [4]), as the measurements were conducted at temperatures below the Néel temperature for these samples. The upper edge of the valence band (VB) shows weak intensity and is ambiguously defined, schematically indicated by a wide rectangle.

As the concentration of the substituent increases, the edges of the VB and CB converge, indicating a decrease in the bulk band gap (panels b and f). Additionally, the width of the states increases, appearing more blurred, likely due to the introduction of additional electron scattering centers. Furthermore, parabolic states, which split along the wave vector relative to the Γ-point (Rashba-like states), appear in the spectra. These states are present in $MnBi_2Te_4$ but are strongly hybridized with the CB states and located near the Fermi level, making them poorly distinguishable in the spectra. With increasing Mn substitution, these states shift towards higher binding energies and become more distinct.

The topological phase transition for the mixed crystals with all three elements is expected within the substitution range of approximately 40-60% [9,11]. In the case of Mn substitution by Sn (panel g, 52 %), there is a notable weakening of the VB states' intensity. The Rashba-like states become the most intense in the CB. For Mn substitution by Pb (panel k, 49 %), the edge of the CB (a parabolic state with a binding energy around 0.27 eV) can be identified in the spectrum. The VB states also exhibit weak intensity, making it difficult to distinguish their edge. Generally, it can be observed that the spectra in panels (g) and (k) do not show states corresponding to TSS, nor do they display a cone of bulk states. In the case of Mn substitution by Ge (panel c, 45 %), at studied concentration conical states can still be identified and attributed to TSS.

At substitution concentrations of approximately 80% or higher (panels d, h, l), the electronic structure of the mixed crystals becomes similar to that of $GeBi_2Te_4$, $SnBi_2Te_4$, or $PbBi_2Te_4$, respectively. The transition from the $MnBi_2Te_4$-like electronic structure to these electronic structures is abrupt, with no smooth modification of states. In the spectra, when compared with literature data, one can identify the TSS as narrow, intense states. These TSS are significantly distorted near the upper edge of the VB, with the Dirac point located within the VB region.

Thus, with the substitution of Mn by nonmagnetic elements Ge, Sn, and Pb, a distinct change in the electronic structure is observed. This change likely involves a transition from the TI phase to a trivial insulator phase, and then back to a TI phase with a different topological Z_2 invariant. The transition between the TI and trivial insulator phases may occur through a Dirac semi-metal phase, which is likely to be observed only within a very narrow range of substitution concentrations. Overall, the trend in the electronic structure modification is almost identical for all three non-magnetic elements. Minor differences, such as the positions of the Dirac point or the width of the TSS, are likely attributed to the specific synthesis conditions of each crystal.

REFERENCES

1. Y. Tokura, et al., *Nature Reviews Physics* **1**, p. 126, 2019.
2. B.A. Bernevig, et al., *Nature* **603**, p. 41, 2022.
3. M. M. Otrokov, et al., *Nature* **576**, p. 416, 2019.
4. D. A. Estyunin, et al., *APL Materials* **8**, p. 021105, 2020.
5. Y. Hao, et al., *Phys. Rev. X* **9**, p. 041038, 2019.
6. A. M. Shikin, et al., *Phys. Rev. B* **104**, p. 115168, 2021.
7. M. Garnica, et al., *Quantum Materials* **7**, p. 7, 2022.
8. J. Zhu, et al., *Phys. Rev. B* **103**, p. 144407, 2021.
9. T. Qian, et al., *Phys. Rev. B* **106**, p. 045121, 2022.
10. D. A. Estyunin, et al., *Magnetochemistry* **9**, p. 210, 2023.
11. A. S. Frolov, et al., *Communications Physics* **7**, p. 180, 2024.

Observation of electron structure of chiral magnet $YbNi_3Al_9$ by ARPES

Y. Tanimoto[a], M. Sugimoto[a], Y. Nakashima[b], H. Sato[c], Y. Miyai[c],
S. Ideta[c], K. Shimada[c], S. Nakamura[d], S. Ohara[d]

[a]*Graduate School of Advanced Science and Engineering, Hiroshima University, Higashi-Hiroshima 739-8526, Japan*
[b]*Faculty of Science, Hiroshima University, Higashi-Hiroshima 739-8526, Japan*
[c]*Hiroshima Research Institute for Synchrotron Radiation Science, Hiroshima University, Higashi-Hiroshima 739-0046, Japan*
[d]*Graduate School of Engineering, Nagoya Institute of Technology, Nagoya 466-8555, Japan*

Keywords: chiral magnetic crystal, helical magnetism, angle resolved photoemission spectroscopy

Trigonal $YbNi_3Al_9$ has attracted interest as the first chiral magnetic alloy discovered among 4*f* electron systems [1]. The Yb 4*f* spins become magnetically ordered below T=3.4 K, exhibiting either left-handed or right-handed helical magnetism with a propagation vector of $\boldsymbol{q} = (0, 0, 0.8)$ [2]. In this study, angle-resolved photoemission spectroscopy (ARPES) was performed on $YbNi_3Al_9$ to investigate the conduction electron band structure near the Fermi level (E_F). Single crystals used for the ARPES measurements were synthesized using the flux-method [3]. The experiments were conducted at BL-1 of Hiroshima Research Institute for Synchrotron Radiation Science, Hiroshima University.

Figures 1 (a), (b) and (c) show the ARPES intensity plots of $YbNi_3Al_9$ measured at $h\nu$=40, 58 and 92 eV, respectively, with *p*-polarized geometry along the $\bar{\Gamma}$-$\bar{K}$ directions of the surface Brillouin zone, respectively. Several hole-like bands around the $\bar{\Gamma}$ point crossing E_F are observed and exhibit dispersion along k_z direction. Additionally, a parabolic band with an upward curvature, centered at the $\bar{\Gamma}$ point with a top near E_F, is observed. Comparison with the results of the soft x-ray ARPES is now in progress.

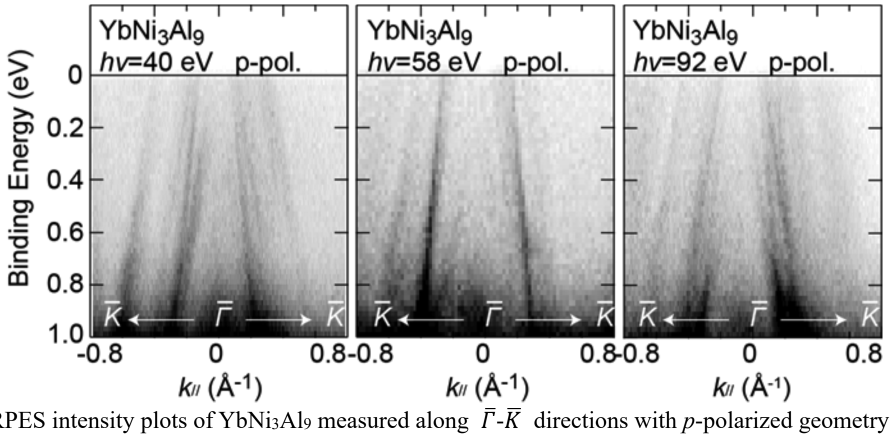

Fig. 1. ARPES intensity plots of $YbNi_3Al_9$ measured along $\bar{\Gamma}$-$\bar{K}$ directions with *p*-polarized geometry at photon energies of (a) $h\nu$=40 eV, (b) 59 eV and (c) 92 eV.

REFERENCES

1. S. Ohara, S. Fukuta, K. Ohta, H. Kono, T. Yamashita, Y. Matsumoto and J. Yamaura, JPS Conf. Proc. **3**, 017016 (2014).
2. T. Matsumura, Y. Kita, K. Kubo, Y. Yoshikawa, S. Michimura, T. Inami, Y. Kousaka, K. Inoue and S. Ohara, J. Phys. Soc. Jpn. **86**, 124702 (2017).
3. T. Yamashita, R. Miyazaki, Y. Aoki and S. Ohara, J. Phys. Soc. Jpn. **81**, 034705 (2012).

Evidence for Two-dimensional Weyl Fermions in Air-Stable Monolayer PtTe1.75

Zhihao Cai,[a,b,#] Haijun Cao,[a,b,#] Haohao Sheng, [a,b] Xuegao Hu, [a,b] Zhenyu Sun, [a,b] Qiaoxiao Zhao, [a,b] Jisong Gao, [a,b] Shin-ichiro Ideta,[c] Kenya Shimada,[c] Jiawei Huang,[d] Peng Cheng, [a,b] Lan Chen, [a,b,d*] Yugui Yao,[e] Sheng Meng, [a,b,d,f*] Kehui Wu, [a,b,d,f*] Zhijun Wang, [a,b] Baojie Feng [a,b,d,f*]

[a]Institute of Physics, Chinese Academy of Sciences, Beijing, 100190, China
[b]School of Physical Sciences, University of Chinese Academy of Sciences, Beijing, 100049, China
[c]Hiroshima Synchrotron Radiation Center, Hiroshima University, Higashi-Hiroshima 739-0046, Japan
[d]Songshan Lake Materials Laboratory, Dongguan, Guangdong, 523808, China
[e]Centre for Quantum Physics, Key Laboratory of Advanced Optoelectronic Quantum Architecture and Measurement (MOE), School of Physics and Beijing Key Lab of Nanophotonics Ultrafine Optoelectronic Systems, School of Physics, Beijing Institute of Technology, Beijing 100081, China
[f]Interdisciplinary Institute of Light-Element Quantum Materials and Research Center for Light-Element Advanced Materials, Peking University, Beijing, 100871, China
#These authors contributed equally to this work.
**Corresponding author. E-mail: lchen@iphy.ac.cn; smeng@iphy.ac.cn; khwu@iphy.ac.cn; bjfeng@iphy.ac.cn.*

Keywords: 2D Weyl fermions, monolayer $PtTe_{1.75}$, ARPES, SHG, DFT calculations

Topological semimetals, including Dirac, Weyl, and nodal line semimetals, are characterized by linearly dispersing bands that intersect at discrete points or extended lines [1]. Among topological semimetals, Weyl semimetals are particularly captivating [2]. Unlike Dirac and nodal line semimetals, Weyl semimetals only need translational symmetry of the crystal, which makes them more resistant to external perturbations. To date, a variety of three-dimensional crystals have been found to host Weyl fermions, exemplified by TaAs [3], WTe_2 [4], and $Co_3Sn_2S_2$ [5], and they exhibit a range of exotic transport and optical properties.

Meanwhile, research on two-dimensional (2D) materials has boomed due to the ongoing trend of device miniaturization. Recently, several candidate 2D Weyl semimetals have been theoretically predicted, but synthesis of these materials is challenging, which hinders their experimental investigation.

Here, we present experimental evidence for 2D Weyl fermion states in a non-centrosymmetric 2D material, the monolayer $PtTe_{1.75}$, by combined angle-resolved photoemission spectroscopy (ARPES), scanning tunneling microscopy (STM), second harmonic generation (SHG), X-ray photoelectron spectroscopy (XPS) measurements, and first-principles calculations. The strong spin-orbit coupling (SOC) and lack of inversion symmetry give rise to three pairs of Weyl nodes in the first BZ. The linearly dispersing Weyl cones have been directly observed by systematic ARPES measurements, substantiated by first-principles calculations. In addition, monolayer $PtTe_{1.75}$ is extremely stable in various environments, including air, alcohol, and acetone, as sharp low-energy electron diffraction (LEED) patterns survive without degassing in vacuum. Our results establish monolayer $PtTe_{1.75}$ as an ideal platform to investigate the intriguing properties of Weyl fermions in the 2D limit.

The band structure of monolayer $PtTe_{1.75}$ is shown in Fig. 1d. Because of the strong SOC and absence of inversion symmetry, a giant Rashba splitting occurs at the Γ point, as indicated by the red circle in Fig. 1d. The spin-split bands are inverted, forming a twofold degenerate critical Weyl point in the $M_{100}*T$ invariant line Γ-K, as indicated by the red arrow in Fig. 1d. The validity of Weyl points has also been confirmed by our Berry curvature calculations, as shown in Fig. 1e. To reveal the spin polarization of the Weyl cone, we calculated the spin texture of $PtTe_{1.75}$ with SOC, as shown in Fig. 1(f-h).

Monolayer PtTe$_{1.75}$ can be synthesized by growing Te on the Pt(111) substrate [6]. Notably, the bulk bands of Pt(111) have stronger spectral weights near the BZ boundary of Pt(111), where they overlap with the bands of PtTe$_{1.75}$. To clearly resolve the band structures of the PtTe$_{1.75}$, we focus on the band structure in the first BZ, where the bulk bands of Pt(111) have less spectral weight. Figure 3a illustrates the distribution of the six Weyl nodes and the momentum cuts along which ARPES spectra were acquired. Along the Γ-K direction, linearly dispersing bands with a cone-like shape were observed, as indicated by the black arrows in Fig. 3b. The band degenerate point is located at approximately 0.4 eV below the Fermi level. Along the perpendicular direction, *i.e.*, Cut AB, linearly dispersing bands with a crossing point at 0.4 eV were also observed, as shown in Fig. 3e. These results fully agree with the existence of six Weyl cones in the first BZ of PtTe$_{1.75}$.

To further confirm the 2D character of the Weyl cone in PtTe$_{1.75}$, we present ARPES spectra along the Γ-K direction measured with different photon energies, as shown in Fig. 3f-3g. The Weyl cones have negligible dispersion with photon energies, which agrees with their 2D character. In contrast, the nearby bulk bands of Pt(111) show apparent dispersion with photon energies. These results provide further evidence for the existence of 2D Weyl cones in monolayer PtTe$_{1.75}$.

As monolayer PtTe$_{1.75}$ is grown on Pt(111), the substrate-overlayer interaction is non-negligible. To clarify the influence of the substrate, we carried out first-principles calculations including the Pt(111) substrate. Figure 3d displays the calculated band structure along the Γ-K direction. The Weyl points moved to below the Fermi level because of the electron doping from the substrate. In general, the calculated band structures agree well with our experimental results, as indicated by the black dashed lines in Fig. 3d.

In conclusion, our combined experimental and theoretical results provide evidence for the existence of 2D Weyl fermions in monolayer PtTe$_{1.75}$. Because of the strong spin-orbit coupling and lack of inversion symmetry, monolayer PtTe$_{1.75}$ hosts a giant Rashba splitting and band inversion, giving rise to three pairs of Weyl cones. Combined ARPES measurements and first-principles calculations confirmed the presence of 2D Weyl cones. In addition, our LEED, XPS, and ARPES measurements show that monolayer PtTe$_{1.75}$ has excellent stability in various chemical environments, which is superior to most surface structures and 2D materials.

The paper that includes these data was recently accepted by Nano Letters. A preprint can be found at arXiv:2407.20606 (2024).

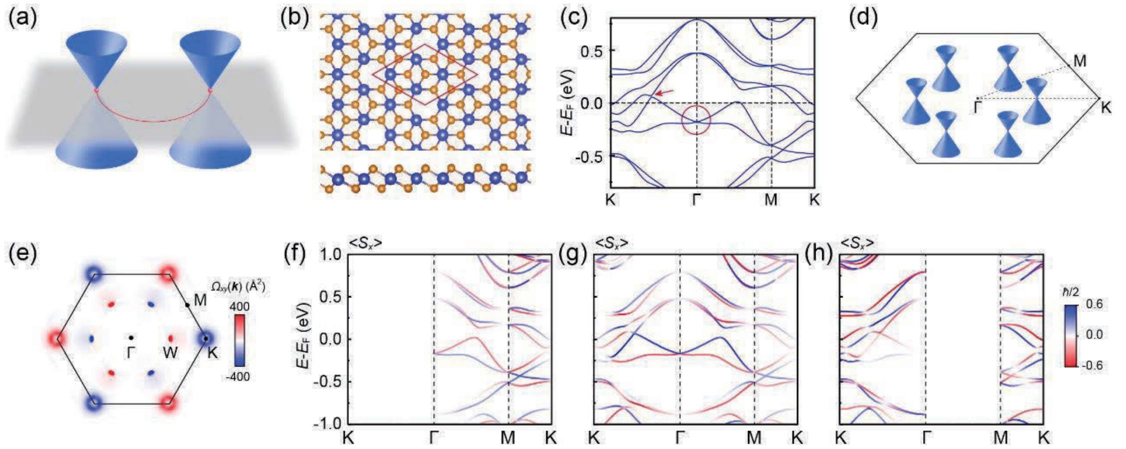

FIGURE 1: Overview of 2D Weyl fermions and monolayer PtTe$_{1.75}$. (a) Schematic drawing of a pair 2D Weyl cones. There are topological edge states connecting the Weyl nodes, akin to the topological Fermi arcs in 3D Weyl semimetals. (b) Top view and side view of the structure model of monolayer PtTe$_{1.75}$. Orange and blue balls represent the Te and Pt atoms, respectively. The red rhombus indicates a unit cell. (c) Calculated band structure of monolayer PtTe$_{1.75}$ with SOC. The red circle indicates the Rashba splitting at the Γ point. The red arrow indicates Weyl cones between the Γ and K point. (d) The distribution of the Weyl cones in the first BZ. (e) The distribution of Berry curvature of freestanding monolayer PtTe$_{1.75}$. (f-h) Calculated spin texture in freestanding monolayer PtTe$_{1.75}$.

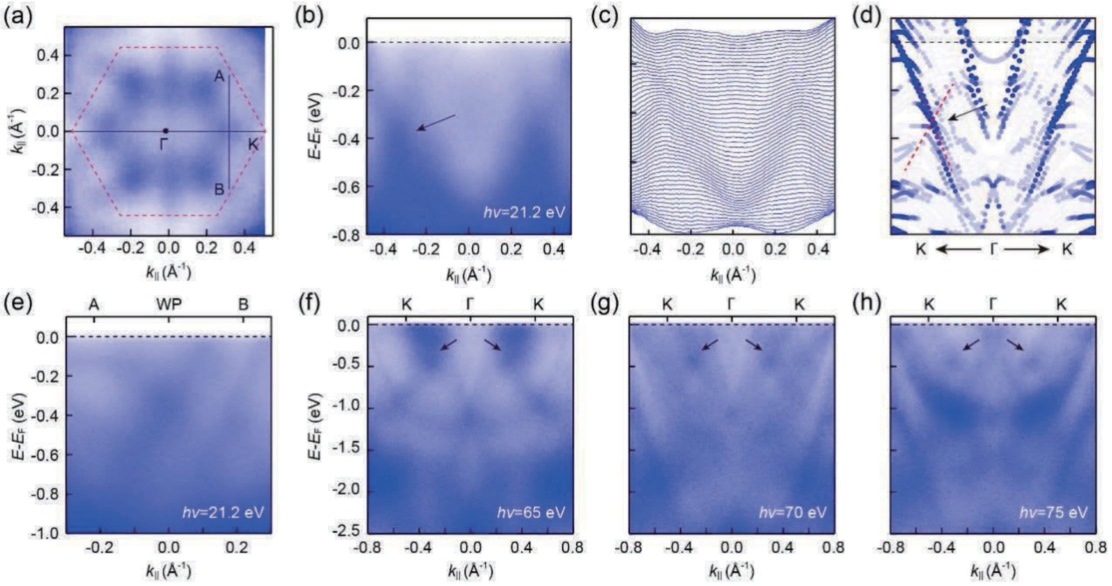

FIGURE 3: ARPES measurement of the band dispersion. (a) Constant energy contour of monolayer $PtTe_{1.75}$ at 0.4 eV. The red dashed line indicates the first BZ of $PtTe_{1.75}$. (b) ARPES intensity plots along the K-Γ-K direction of $PtTe_{1.75}$/Pt(111). (c) Momentum distribution curves extracted from (b). (d) DFT calculated band structure of $PtTe_{1.75}$/Pt(111) along the K-Γ-K direction. (e) ARPES intensity plots along Cut AB, as indicated in (a). (f-h) Photon energy dependent band dispersion of $PtTe_{1.75}$/Pt(111). Black arrows indicate the Weyl cones, which shows negligible dispersion with photon energy.

REFERENCES

1. Bernevig, B. A.; Felser, C.; Beidenkopf, H. Progress and prospects in magnetic topological materials. Nature 2022, 603, 41-51.
2. Xu, S.-Y.; Belopolski, I.; Alidoust, N.; Neupane, M.; Bian, G. Zhang, C.; Sankar, R.; Chang, G.; Yuan, Z.; Lee, C.-C.; Huang, S.-M.; Zheng, H.; Ma, J.; Sanchez, D. S.; Wang, B.; Bansil, A.; Chou, F.; Shibayev, P. P.; Lin, H.; Jia, S.; Hasan, M. Z. Discovery of a Weyl fermion semimetal and topological Fermi arcs. Science 2015, 349, 613-617.
3. Lv, B. Q.; Weng, H. M.; Fu, B. B.; Wang, X. P.; Miao, H.; Ma, J.; Richard, P.; Huang, X. C.; Zhao, L. X.; Chen, G. F.; Fang, Z.; Dai, X.; Qian, T.; Ding, H. Experimental discovery of Weyl semimetal TaAs. Phys. Rev. X 2015, 5, 031013.
4. Soluyanov, A. A.; Gresch, D.; Wang, Z.; Wu, Q.; Troyer, M.; Dai, X.; Bernevig, B. A. Type-II Weyl semimetals. Nature 2015, 527, 495-498.
5. Liu, E.; Sun, Y.; Kumar, N.; Muechler, L.; Sun, A.; Jiao, L.; Yang, S.-Y.; Liu, D.; Liang, A.; Xu, Q.; Kroder, J.; Süß, V.; Borrmann, H.; Shekhar, C.; Wang, Z.; Xi, C.; Wang, W.; Schnelle, W.; Wirth, S.; Chen, Y.; Goennenwein, S. T. B.; Felser, C. Giant anomalous Hall effect in a ferromagnetic kagome-lattice semimetal. Nat. Phys. 2018, 14, 1125-1131.
6. Liu, L.; Zemlyanov, D.; Chen, Y. P. Epitaxial growth of monolayer PdTe2 and patterned PtTe2 by direct tellurization of Pd and Pt surfaces. 2D Mater. 2021, 8, 045033.

Mapping the Pseudospin Texture in a Kagome Superconductor by means of Dichroic ARPES

Begmuhammet Geldiyev[a], Philipp Kagerer[a], Jakub Schusser[a], Noah Endres[a],
Yudai Miyai[b], Yogendra Kumar[b], Shin-ichiro Ideta[b], Kenya Shimada[b,c],
Maximilian Ünzelmann[a], and Friedrich Reinert[a]

[a]Experimentelle Physik VII and Würzburg-Dresden Cluster of Excellence ct.qmat
Universität Würzburg, Am Hubland, D-97074 Würzburg, Germany
[b]Research Institute for Synchrotron Radiation Science
Hiroshima University, 2-313 Kagamiyama, Higashi-Hiroshima, Hiroshima 739-0046, Japan
[c]International Institute for Sustainability with Knotted Meta Matter (WPI-SKCM^2)
Hiroshima University, 2-313 Kagamiyama, Higashi-Hiroshima, Hiroshima 739-0046, Japan

Keywords: Kagome superconductors, orbital pseudospin, light-polarization-dependent ARPES

In the recent decade, research on Kagome metals – featuring the simultaneous emergence of exciting physical phenomena such as superconductivity, chiral charge order, and topology in the same host – garnered tremendous attention [1]. Particularly, the family of materials with chemical composition AV_3Sb_5 (A = K, Rb, Cs) remains in the spotlight [2-4].

Similar to the case in graphene [5,6], a particular pseudospin observable stemming from certain sublattice degree of freedom (DOF) plays an important role also for Kagome networks. In addition, the orbital pseudospin component becoming relevant as the consequence of five V-3*d* orbitals located at each Kagome lattice site, making the single-orbital picture to be obsolete. Moreover, the Fermi surfaces in the AV_3Sb_5 class of materials are not only built from Kagome-related (i.e. V-3*d*) states (see purple arrow in Fig. 1), but also electron-like Sb-p_z bands (green arrows in Fig. 1) contribute to complex band manifolds [3] and are thus likely decisive for the physical properties. In this regard, it becomes quintessential to comprehend the pseudospin physics in these materials in detail.

In order to address these aspects experimentally, we employed ARPES with variable linear light polarization. This means, we acquired momentum maps with a fixed sample orientation and use the ability of the rotatable ARPES system at BL-1 to change the linear light polarization gradually from p ($\gamma = 0°$)- to s ($\gamma = 90°$) polarization after each measurement. Such an exemplary measurement series is shown in Fig. 1(a). The constant energy cuts clearly show the Kagome-related V-3*d* bands particularly around the K points as well as the Sb-p_z electron pocket at the zone center. Overall, one finds a prominent left-right asymmetry if there is a finite contribution of *p*-polarization in the light electric field vector, which in consequence drops gradually in the four datasets shown. This asymmetry is referred to as linear dichroism (LD) [7-10] which can give access to the orbital angular momentum (OAM) in the initial state wave function [7,10]. Fig. 1(c) shows the LD = $I(+k_x,k_y) - I(-k_x,k_y)$ extracted from an ARPES measurement taken with purely p polarized light ($\gamma = 0°$). One finds an interesting and complex LD pattern in both the V-3*d* and the Sb-p_z bands. Overall, the concrete origin is presently under investigation [11] and will be supported by SPR-KKR photoemission calculations and circular dichroism measurements [12]. One particular interesting aspect could be a surface-induced formation in the bulk bands of the inversion symmetric material. In order to elaborate on this aspect we model our experimental data i.e. especially the Sb-p_z electron pocket, by simple model calculations assuming an OAM-carrying band (marked by the green arrow in Fig.1). In this we find the mixing of out-of-plane p_z with radial aligned in-plane $p_{x,y}$ orbitals (which lead to the formation of OAM L_y) to be responsible for the calculated LD (Fig.1(c)). In the experiments, we could not only address the OAM via LD but also this particular orbital texture. In the polarization series in Fig.1(a), we find the intensity distribution of the Sb-band to develop from almost uniform, when p polarized light is used, to a rotating dumbbell shape. When light is completely s polarized (and thus exclusively sensitive to in-plane orbitals), the observed pattern is entirely two-fold symmetric. This resembles a radial in-plane orbital alignment [7] and the complete series is nicely reproduced by the simple model simulations.

In summary, we have studied the pseudospin texture of a Kagome-type quantum material CsV$_3$Sb$_5$ using linear dichroism as well as polarization-modulated ARPES, i.e. two approaches that have been proposed to provide information about the pseudospin texture [7,10,13]. Supported by simple model simulations of the photoemission intensity, our results hint towards a surface-induced formation of OAM in the bulk bands of the inversion symmetric compound [11], which – to the best of our knowledge – has not been reported so far.

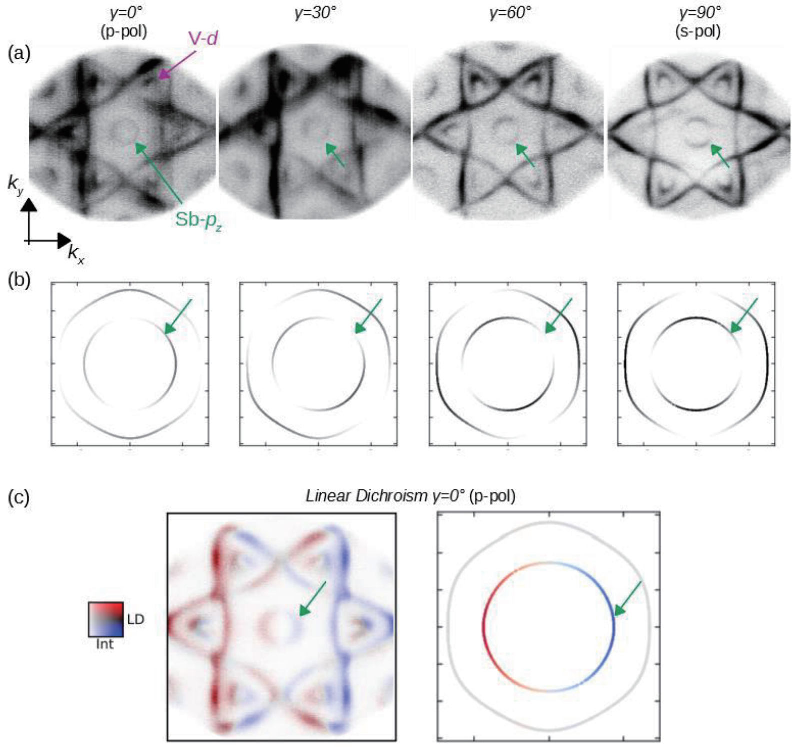

FIGURE 1. Overview of polarization-dependent ARPES measurements. (a) Constant energy contours (CECs) recorded with a photon energy of 78 eV at approximately 180 meV binding energy (the upper section of the Kagome Dirac cone (purple arrow). Here we focus on the circular feature located at the center of CECs (indicated by the green arrows) which as predominantly Sb-p_z character. Upon gradual evolution of light polarization from p $(\gamma = 0^\circ)$ to s $(\gamma = 90^\circ)$, which is from left to right, an intensity redistribution is taking place. For p polarization, the intensity is mostly uniform, whereas there is no intensity at $k_x = 0$ lobes at around $k_y = 0$ path for s polarization. (b) Supporting ARPES simulations – representing the Sb-p_z band – where we observe the same behavior for the band with radial-orbital alignment. (c) Linear dichroism (LD) extracted from the same constant energy cuts as in (a) $(\gamma = 0^\circ)$ but taken at a photon energy of 66 eV. On the right hand side, an LD simulation is shown.

REFERENCES

1. T. Neupert et al., *Nat. Phys.* **18**, 137-143 (2022)
2. Y. Hu et al., *Nat. Commun.* **13**, 2220 (2022)
3. M. Kang et al., *Nat. Phys.* **18**, 301-308 (2022)
4. X. Wu et al., *Phys. Rev. Lett.* **127**, 177001 (2021)
5. Y. Liu et al., *Phys. Rev. Lett.* **107**, 166803 (2011)
6. I. Gierz et al., *Nano Lett.* **12**, 3900-3904 (2012)
7. M. Ünzelmann et al., *Phys. Rev. Lett.* **124**, 176401 (2020)
8. H. Bentmann et al., *Phys. Rev. Lett.* **119**, 106401 (2017)
9. C.-H. Min et al., *Phys. Rev. Lett.* **122**, 116402 (2019)
10. T. Figgemeier et al., arXiv:2402.10031 (2024)
11. M. Ünzelmann, J. Schusser, et int., F. Reinert, in preparation (2024)
12. M. Ünzelmann et al., *Nat. Commun.* **12**, 3650 (2021)
13. M. Schüler et al., *Phys. Rev. X* **12**, 011019 (2021)

Observation of band dispersion in Yb intercalated graphene

Ryota Akiyama[a]*, Shunsuke Sato[a], Yudai Miyai[b], Jehong Jung[a], Rei Hobara[a],
Yogendra[b], Amit Kumar[b], Shota Shimizu[a], Ryotaro Minakawa[a],
Shin-ichiro Ideta[b], Kenya Shimada[b], and Shuji Hasegawa[a]

[a] *The University of Tokyo, 7-3-1 Hongo, Bunkyo, Tokyo, 113-0033 Japan*
[b]*Hiroshima University, 1-3-2 Kagamiyama, Higashihiroshima, Hiroshima, 739-0046 Japan*

Keywords: graphene, intercalation, ytterbium, superconductivity, two-dimensional material, 4*f* electrons, van Hove singularity.

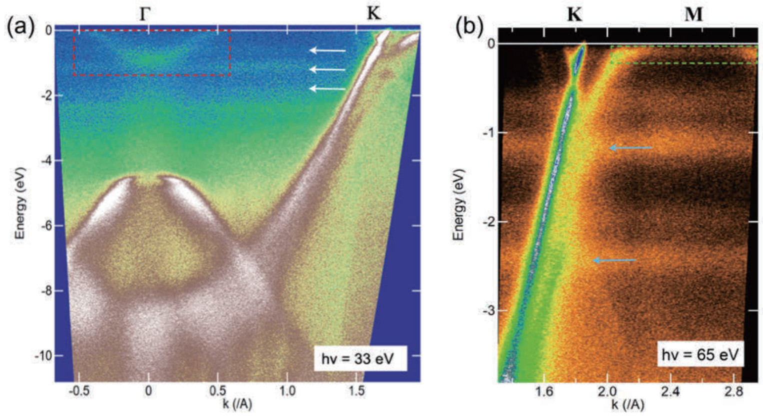

Fig. 1 Band dispersion around (a) Γ and K points, (b) K and M points by observed ARPES

When atoms are intercalated into graphene, the electronic structure changes dramatically due to the regular structure of the intercalant and the long period of the atomic structure, depending on the conditions. We have previously reported superconductivity in Ca [1,2] and ferromagnetism in Yb [3]. However, superconductivity in graphene has not been reported by electrical transport measurements in intercalants other than Ca, and elucidation of the mechanism and realization by further atomic species have been waited for. In such a situation, we have succeeded in achieving superconductivity at T_C=1.5 K by Yb intercalation.[4] Since Yb is a heavier element than Ca and has an anisotropic electron orbital in the 4*f* electron system, it is fascinating to see how it affects superconductivity when intercalated into graphene, since ARPES has been reported to create hybridized orbitals of the Yb 4*f* level and graphene, unconventional types of superconductivity, such as superconductivity with nodes, are also expected. In addition, when the Fermi level is properly tuned, graphene is theoretically expected to have flat band-like van Hove singularity (vHs) band that contributes to superconductivity, and the symmetry of superconductivity is expected to be chiral *d*- or *f*-wave [5].

In this study, we would like to elucidate the nature of ferromagnetism and superconductivity realized by Yb intercalation and clarify how they are correlated. So far, we have clarified the realization of superconductivity and its fundamental electrical properties, as well as the location of Yb and its valence, using electrical conduction and photoelectron holography. Subsequently, ARPES energy dispersion measurements revealed that a $\sqrt{3}\times\sqrt{3}$ superstructure is formed, and the existence of folded bands (red dashed square in Fig. 1(a)). The graphene π^* band and the Yb 4*f* level (white arrows in Fig. 1(a)) hybridize (blue arrows in Fig. 1(b)), indicating the strong influence of the Yb electron orbitals on graphene. In the case of Ca, vHs is far from the Fermi level, but in Yb case, the fact that the valence of Yb is trivalent at the substrate termination and divalent between the graphene layers is thought to be the cause of a good adjustment of vHs. In the future, we would like to further investigate the unconventional nature of superconductivity, its relation to ferromagnetism, and the easy way of Yb intercalation.

REFERENCES

[1] S. Ichinokura *et al.*, ACS Nano **10**, 2761 (2016)
[2] H. Toyama, RA *et al.*, ACS Nano **16**, 3582 (2022).
[3] J. Jung, RA *et al.*, 10pPSB-50, JPS2019 年秋季大会 (2019).
[4] S. Sato, RA *et al.*, 第 78 回日本物理学会年次大会 16pPSA-12 (2023).
[5] M. L. Kiesel *et al.*, Phys. Rev. B **86**, 020507 (2012).

23BG016 BL-1

Synchrotron ARPES studies of nodal line semimetal $LaTe_{1+x}Bi_{1-x}$

Ryusei Saito[a], Yuta Okishi[a], Tomoki Higashikawa[a], Takanori Wakita[a,b] ,
Yogendra Kumar[c], Yudai Miyai[c], Haruka Kageyama[a], Ryusuke Kondo[a],
Yoshio Nogami[a], Shinichiro Ideta[c], Kenya Shimada[c], Yuji Muraoka[a,b],
Takayoshi Yokoya[a,b]

[a]Graduate School of Natural Science and Technology, Okayama University, Okayama 700-8530, Japan
[b]Research Institute for Interdisciplinary Science, Okayama University, Okayama 700-8530, Japan
[c]Hiroshima Synchrotron Radiation Center, Hiroshima University, Higashi-Hiroshima 739-0046, Japan

Keywords: Topological material, Nodal line semimetal, Band dispersion, ARPES

$LaTe_{1+x}Bi_{1-x}$ is a layered material consisting of an insulating layer of LaTe and a conducting Bi square lattice layer. Band calculation predicted that it possesses a Dirac nodal-line along Γ-R in the Brillouin zone (BZ) (Fig. 1) [1], and therefore it can be classified as a nodal line semimetal for which exotic transport properties can be expected [2]. However, predicted nodal line of LaTeBi is located slightly above the Fermi level (E_F). To experimentally observe the nodal line and also determine its energy position relative to E_F are important to investigate the potential of $LaTe_{1+x}Bi_{1-x}$ to exhibit topological physical properties. In this presentation, we report synchrotron angle-resolved photoemission spectroscopy (ARPES) study of $LaTe_{1+x}Bi_{1-x}$, which was performed to directly observe the valence band electronic structure of $LaTe_{1+x}Bi_{1-x}$.

The samples measured were $LaTe_{1+x}Bi_{1-x}$ (x = 0.2) single crystals prepared by the flux method. Synchrotron ARPES experiments were performed by a high-resolution ARPES spectrometer at BL-1 of HiSOR, with linearly polarized light and with the light spot size of 40 (H) x 50 (V) μm. The energy resolution was set to ~ 40 meV and the measurement temperature was 20 K.

Figure 1 shows an ARPES intensity map measured along the ΓX line of the BZ. The black regions correspond to bands. Distinct dispersive bands symmetric with respect to the high symmetry points are clearly observed in the entire energy region shown. The observed bands were found generally consistent with the results of band calculations. Around X, one can find bands approaching E_F.

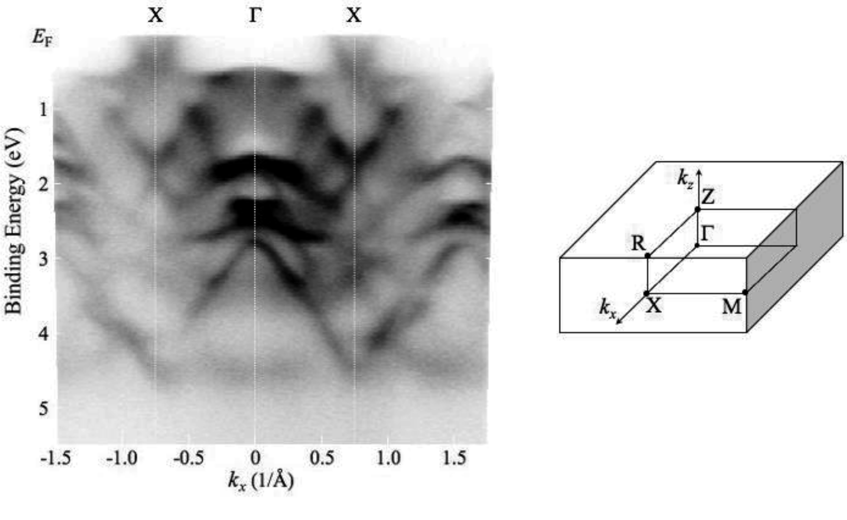

FIGURE 1. ARPES intensity map of $LaTe_{1.2}Bi_{0.8}$ and Brillouin zone

Figure 2 shows a minus second-derivative ARPES intensity map near E_F and around X. “W” shaped dispersive bands symmetric with respect to X are observed. The characteristic dispersion is consistent with calculation, indicating that a nodal line is located very close to E_F at X in $LaTe_{1.2}Bi_{0.8}$.

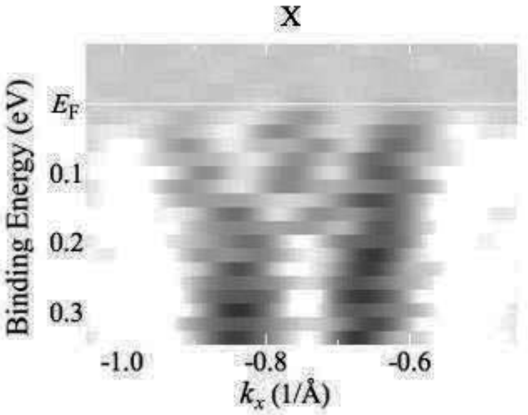

FIGURE 2. Minus second-derivative ARPES intensity map near E_F and around X of $LaTe_{1.2}Bi_{0.8}$

REFERENCES

1. R. Kondo, private communication.
2. C. Feng *et al.*, Chinese Phys. B 25, 117106 (2016).

ARPES Study On Magnetic Hourglass Candidate CsMn2F6

Fayuan Zhang[a] and Chaoyu Chen[a]

[a] *Shenzhen Institute for Quantum Science and Engineering, Southern University of Science and Technology, Shenzhen, China.*

Keywords: Magnetic Hourglass Fermions, ARPES.

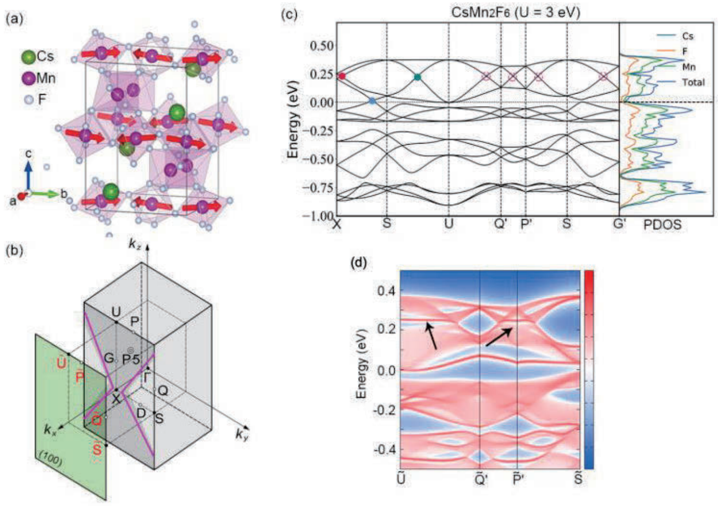

FIGURE 1. (a) The crystal and magnetic structure of CsMn2F6, (b) The BZ of CsMn2F6 and the (100) surface BZ, (c) The electronic band structure of CsMn2F6 and the plot of density of states (with U= 3 eV). (d) results for surface states indicated by the red color: The black arrow denotes the associated drumhead surface states.

As a new type of quasiparticle, hourglass fermion has received extensive attention.[1, 5-9] Under the protection of nonsymmorphic symmetries hourglass-like surface states can be formed, the states at the neck point of the hourglass-type dispersion are referred to as hourglass fermions. This concept of novel topological state make it possible to investigate hourglasss Weyl chains[10], hourglass Dirac chain[11] and hourglass nodal net[12] semimetals. KHgX (X = As, Sb, Bi)[1, 2], M3SiTe6 (M = Nb, Ta)[3, 4] and ErAsS[13] have been confirmed as the hourglass fermion candidates protected by nonsymmorphic symmetries (Fig. 1(c)-(e)), it is predicted that doubled quantum spin Hall effect (DQSHE) can be realized on the (100) surface of KHgX, DQSHE as a novel transportation has two pairs of surface mode with opposite spin polarization and propagating direction. Although there are many predictions, for instance, perovskite iridates[14] and other oxides[10-12] are also predicted to hold hourglass-type dispersions, there is very little experimentally confirmed materials. Studies are mainly focused on non-magnetic materials in the past, while studies on magnetic hourglass fermion candidates may give a broader platform to realize DQSHE. Recently, a theoretical study predicted that antiferromagnet CsMn2F6[15] holds the hourglass band structure around the Fermi level and the topologically protected surface drumhead states of (100) surface are found to spread over more than one half surface Brillouin zone and only appear within ~30 meV energy window[16], as shown in Fig. 1, the prominent electronic correlation could induce intriguing stability. Experimental investigation is essential to unveil the band structure of CsMn2F6.

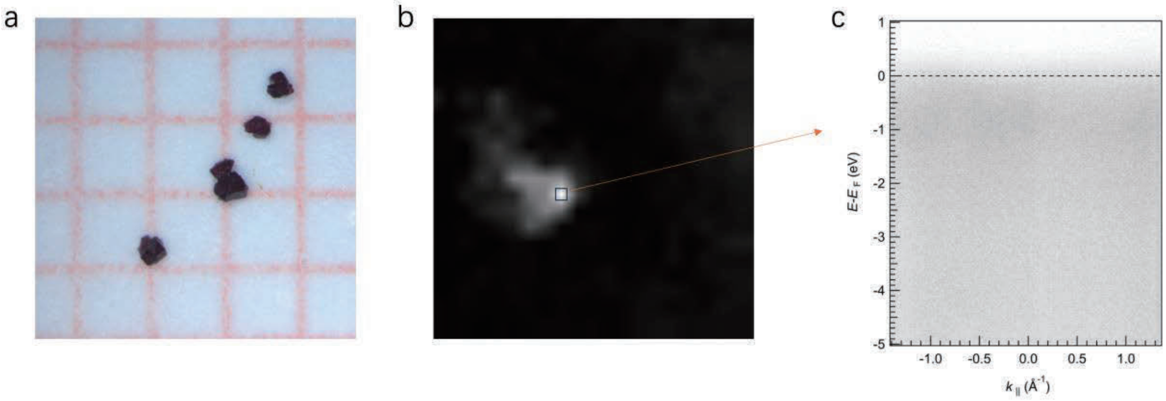

FIGURE 2. (a) The photos of CsMn2F6, (b) The real space photoemission spectral intensity mapping of CsMn2F6. (c) The corresponding photoemission spectra from the spot indicated in (b).

Based in the ARPES endstation at BL1 of HiSOR, we have cleaved several CsMn2F6 single crystals and tried to find the signature of band structure. While we can locate the cleaved surface properly, we could not find any band feature, as shown by the quite flat spectral intensity in Figure 2c. We suspect that the strong correlation in CsMn2F6 makes the quasiparticle band incoherent.

REFERENCES

[1] Wang, Z., et al., Hourglass fermions. Nature, 2016. 532(7598): p. 189-94.
[2] Ma, J., et al., Experimental evidence of hourglass fermion in the candidate nonsymmorphic topological insulator KHgSb. Science Advances, 2017. 3(5): p. e1602415.
[3] Li, S., et al., Nonsymmorphic-symmetry-protected hourglass Dirac loop, nodal line, and Dirac point in bulk and monolayer X3SiTe6 (X = Ta, Nb). Physical Review B, 2018. 97(4).
[4] Sato, T., et al., Observation of band crossings protected by nonsymmorphic symmetry in the layered ternary telluride Ta3SiTe6. Physical Review B, 2018. 98(12).
[5] Singh, B., et al., Topological Hourglass Dirac Semimetal in the Nonpolar Phase of Ag2BiO3. Physical Review Letters, 2018. 121(22): p. 226401.
[6] Nam, T.S., et al., Topological bulk band structures of the hourglass and Dirac nodal-loop types in Ce Kondo systems: CeNiSn, CeRhAs, and CeRhSb. Physical Review B, 2019. 99(12).
[7] Zeng, Y., L. Wang, and D.-X. Yao, n-hourglass Weyl fermions in nonsymmorphic materials. Physical Review B, 2020. 101(11).
[8] Zhang, H., et al., Three-dimensional Weyl hourglass networks in the nonsymmorphic half-metal Mg2VO4. Physical Review B, 2020. 102(15).
[9] Zhang, T., et al., BaHgSn: A Dirac semimetal with surface hourglass fermions. Physical Review B, 2020. 101(11).
[10] Chen, C., et al., Weyl-loop half-metal in Li3(FeO3)2. Physical Review B, 2019. 99(7).
[11] Wang, S.S., et al., Hourglass Dirac chain metal in rhenium dioxide. Nature Communications, 2017. 8(1): p. 1844.
[12] Fu, B., et al., Hourglasslike nodal net semimetal in Ag2BiO3. Physical Review B, 2018. 98(7).
[13] Chen, H., et al., Topological Crystalline Insulator Candidate ErAsS with Hourglass Fermion and Magnetic-Tuned Topological Phase Transition. Advanced Materials, 2022. 34(31): p. e2110664.
[14] Chen, Y., Y.M. Lu, and H.Y. Kee, Topological crystalline metal in orthorhombic perovskite iridates. Nature Communications, 2015. 6: p. 6593.
[15] Klepov, V.V., et al., Chloride Reduction of Mn(3+) in Mild Hydrothermal Synthesis of a Charge Ordered Defect Pyrochlore, CsMn(2+)Mn(3+)F(6), a Canted Antiferromagnet with a Hard Ferromagnetic Component. J Am Chem Soc, 2021. 143(30): p. 11554-11567.
[16] Hu, Y., X. Wan, and F. Tang, Magnetic hourglass fermions: From exhaustive symmetry conditions to high-throughput materials predictions. Physical Review B, 2022. 106(16).

Exploration of the topological surface state gap in $Mn(Sb_xBi_{1-x})_4Te_7$

Yu-Jie Hao[a], Xiao-Ming Ma[a], Ruie Lu[a], Ke Zhang[b], Chang Liu[a]

[a] *Shenzhen Institute for Quantum Science and Engineering (SIQSE) and Department of Physics, Southern University of Science and Technology (SUSTech), Shenzhen 518055, China.*
[b] *Hiroshima Synchrotron Radiation Center, Hiroshima University, Higashi-Hiroshima, Hiroshima 739-0046, Japan*

Keywords: surface state, $Mn(Sb_xBi_{1-x})_4Te_7$, ARPES

Magnetic topological quantum materials have attracted widespread attention due to their enormous potential in emerging topological quantum phenomena, such as the quantum anomalous Hall effect (QAHE) [1, 2] and quantum axion electrodynamics [3]. Among these materials, $MnBi_2Te_4$ stands out as the first intrinsic antiferromagnetic topological insulator (AFM TI) [4-6]. Remarkably, QAHE has been observed in five septuple layer (SL) $MnBi_2Te_4$ devices [7]. Antiferromagnetic exchange interaction between adjacent $MnBi_2Te_4$ layers limits QAHE to odd-layer thin films. For even-layer films, achieving quantum Hall plateau requires tuning the magnetism to a ferromagnetic (FM) state via an external magnetic field.

To improve the conditions for observing QAHE, researchers have explored the possibility of regulating the magnetic interaction in $MnBi_2Te_4$ through doping. Specifically, substituting Bi with Sb in $MnBi_2Te_4$ can effectively modulate the magnetic exchange interaction between layers. Our previous experiments on $Mn(Sb_xBi_{1-x})_2Te_4$ at HiSOR demonstrated that Sb doping not only shifts the Fermi level but also opens a gap in the topological surface state. In the $(MnBi_2Te_4)(Bi_2Te_3)_n$ ($n = 0, 1, 2, ...$) family of magnetic topological materials, $MnBi_4Te_7$ ($n = 1$) also exhibits an AFM-TI ground state. Compared to $MnBi_2Te_4$ ($n = 0$), $MnBi_4Te_7$ features a significantly reduced saturation magnetic field (H_{sf}), dropping from 3.6 T [8] to about 0.22 T [9]. This reduction suggests that the evolution of surface states similar to those observed in $Mn(Sb_xBi_{1-x})_2Te_4$ might be detectable when examining $Mn(Sb_xBi_{1-x})_4Te_7$ with specific doping ratios. The low saturation field and the superlattice structure of $MnBi_4Te_7$ make it an ideal candidate for investigating a range of emergent phenomena.

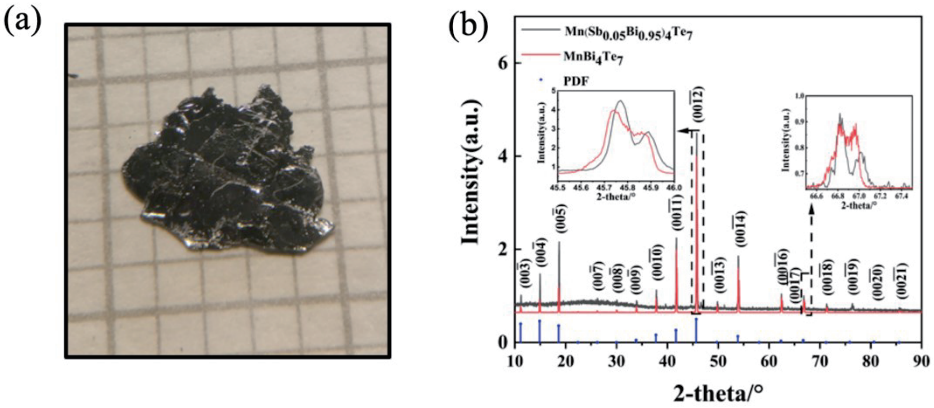

FIGURE 1. Single crystal photo of $Mn(Sb_xBi_{1-x})_4Te_7$ and associated XRD results. (a) A $Mn(Sb_{0.05}Bi_{0.95})_4Te_7$ single crystal against a millimeter grid. (b) XRD results of $MnBi_4Te_7$ and $Mn(Sb_{0.05}Bi_{0.95})_4Te_7$, insets show the detailed peaks of undoped and doped samples for comparison. After doping 5% Sb, the 2θ of ($00\underline{12}$) and ($00\underline{17}$) change to high values, demonstrating the successful doping.

To explore these possibilities, we grew single crystals of $Mn(Sb_{0.05}Bi_{0.95})_4Te_7$ and characterized them using X-ray diffraction (see Figure 1). We intended to use laser-based angle-resolved photoelectron spectroscopy (ARPES) to measure the electronic band structure. Unfortunately, the doping process compromised the crystal quality, leading to insufficiently flat surfaces during cleavage and unclear band structures. As a result, we were unable to confirm the presence of an energy gap in the topological surface states of the Sb-doped $MnBi_4Te_7$ material. Figure 2 presents the band structure of $Mn(Sb_{0.05}Bi_{0.95})_4Te_7$ samples from two different terminations.

In the future, to effectively investigate the topological surface state gap in $Mn(Sb_xBi_{1-x})_4Te_7$, we will optimize our crystal growth techniques to enhance the quality of $Mn(Sb_xBi_{1-x})_4Te_7$ single crystals. Building on the observed immutability of the Fermi level in the $Mn(Sb_{0.05}Bi_{0.95})_4Te_7$ sample, it is essential to synthesize additional samples with higher doping concentrations, such as $x = 0.1$, 0.2, 0.3 and so on. After the synthesis, we plan to apply for additional beam time to measure these higher doped samples.

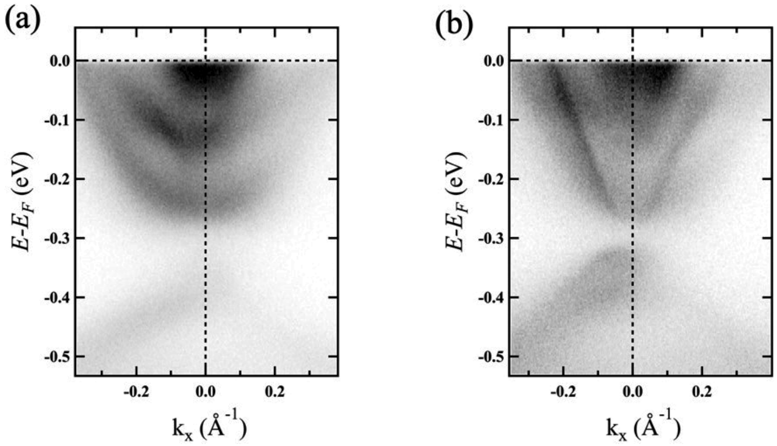

FIGURE 2. ARPES-measured surface states with two different terminations of $Mn(Sb_{0.05}Bi_{0.95})_4Te_7$. (a) The septuple layer ($MnBi_2Te_4$) termination. (b) The quintuple layer (Bi_2Te_3) termination.

REFERENCES

1. R. Yu *et al., Science* **329**, 61 (2010).
2. C.-Z. Chang *et al., Science* **340**, 167 (2013).
3. Xiao *et al., Phys. Rev. Lett.* **120**, 056801 (2018).
4. M. M. Otrokov *et al.*, *Nature* **576**, 416 (2019).
5. Z. S. Aliev *et al.*, *J. Alloys Compd.* **789**, 443 (2019).
6. M. M. Otrokov *et al.*, *Phys. Rev. Lett.* **122**, 107202 (2019).
7. Y. Deng *et al.*, *Science* **367**, 895 (2020).
8. Y.-J. Hao *et al.*, *Phys. Rev. X.* **9**, 041038 (2019).
9. C. Hu *et al.*, *Nat. Commun.* **11**, 97 (2020).

Rashba-like CD pattern of magnetic topological insulators $Mn(Bi_{1-x}Sb_x)_2Te_4$

Meng Zeng[a] and Chang Liu[a]

[a] *Department of Physics and Shenzhen Institute for Quantum Science and Engineering (SIQSE), Southern University of Science and Technology (SUSTech), Shenzhen, Guangdong 518055, China*

Keywords: Dirac cone, topological surface state, magnetic topological insulator, Laser-ARPES, CD-ARPES

The interplay between magnetism and topology give rise to various exotic quantum phenomena such as axion [1-3] and Chern insulating states [4-6], Majorana zero modes [7], and Weyl semi-metallic phase [8-10]. Recently, intrinsic magnetic topological insulator (MTI) has attracted considerable attention due to its great potential in generating high-temperature quantum anomalous Hall effect (QAHE). $MnBi_2Te_4$ is the first intrinsic antiferromagnetic TI [11-13] and has been found to host a variety of exotic quantum states, such as QAHE or axion insulator behavior [14-17]. However, these kind of quantum phenomena are only realized when its crystal thickness is reduced to a few layers, and the theoretically proposed high-temperature QAHE have not yet been observed in bulk samples, indicating that unresolved issues remain in this system.

When using low photon energy ARPES to probe the surface states of $MnBi_2Te_4$, researchers found that the surface states are either gapless [18-20] or have a gap smaller than 15 meV [21], rather than the 88 meV predicted by calculation [15]. This may be the reason for the realization of QAHE at a relatively low temperature in this system. The temperature for the realization of QAHE depends on the size of the Dirac gap [22]. If the gap size can be increased and the Fermi level can be tuned into the bandgap without destroying the topological nature of the surface states, then the QAHE temperature will be significantly improved.

Antimony serves as a convenient dopant in Bi-based topological materials. Recent research found that a relatively small concentration of Sb dopants in $MnBi_2Te_4$ was not only able to raise the gap size up to more than 100 meV, but also shift down the Fermi level, providing a potential platform to observe the high-temperature QAHE [23,24]. However, the underlying mechanism of this anomalous gap is still unclear. Thoroughly measuring the spin texture of the Sb-doped samples by the spin-resolved ARPES may be one of the direct ways to examine whether the nontrivial band topology is preserved in the doped samples [25]. Due to the scarcity of spin-resolved ARPES instruments and insufficient measuring time, we use circular dichroism (CD) ARPES as a measurement technique to indirectly reflect the spin texture of $Mn(Bi_{1-x}Sb_x)_2Te_4$. The CD value in APRES is defined as the difference between the spectrum measured using left circularly polarized light and the one measured using right circularly polarized light, normalized by the sum of the two spectra. CD is sensitive to spins as well as orbital angular momenta [26]. So, researchers usually treat CD-ARPES as a substitute for spin-resolved ARPES.

In this report, we employed laser ARPES at HiSOR to measure $Mn(Bi_{1-x}Sb_x)_2Te_4$ samples with different doping ratio. Our data reveals a Rashba-like CD pattern. First, we perform Fermi mappings and align the $\bar{\Gamma}$ point, then we change the azimuthal angle and make the exit slit parallel to the $\bar{\Gamma}$-$\bar{M}$ direction. The CD-

ARPES results are shown in Fig. 1. For the surface state, the CD patterns at the conduction band minimum and valence band maximum are antisymmetric and does not change with the doping ratio. This behavior is as same as the undoped sample [27], indicating the residual ferromagnetic state at the surface [25]. For the bulk bands, the CD pattern is consistent with the helical spin texture, but at $x = 0.15$, the sign of the pattern is reverse compared to the other two doping concentrations. This could be due to the weak band intensity in the region where the color inversion occurs, which is comparable to the background intensity. The background signal is usually unpatterned.

In the future, we need to measure samples with other doping levels and conduct CD-mapping measurements at some of the samples. This will allow us to more intuitively check the impact of Sb-doping on the spin texture of these magnetic topological insulator system. Additionally, if conditions permit, we will carry out detailed measurements by spin-resolved ARPES and compare the results with the CD pattern shown in this report.

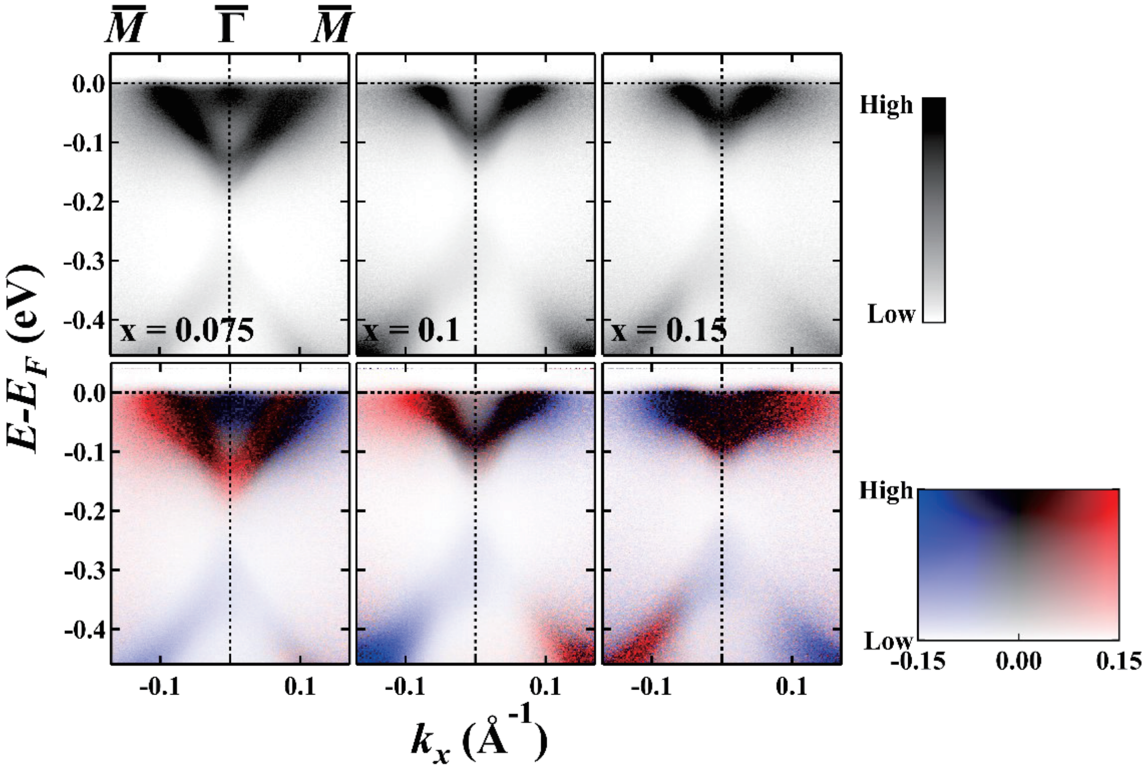

Figure 1. The normal and CD *k*-*E* cuts parallel to $\bar{\Gamma} - \bar{M}$ of $Mn(Bi_{1-x}Sb_x)_2Te_4$ ($x = 0.075, 0.1, 0.15$) at 10 K. Clear Rashba-like CD pattern had been observed.

REFERENCES

1. F. Wilczek. Two applications of axion electrodynamics. Physical Review letters **58**, 1799 (1987).
2. R. S. K. Mong, A. M. Essin, J. E. Moore. Antiferromagnetic topological insulators. Physical Review B **81**, 245209 (2010).
3. R. Li, J. Wang, X. L. Qi, *et al.* Dynamical axion field in topological magnetic insulators. Nature Physics **6**, 284-288 (2010).
4. R. Yu, W. Zhang, H. J. Zhang, *et al*. Quantized anomalous Hall effect in magnetic topological insulators. Science **329**, 61 (2010).
5. C. Z. Chang, J. Zhang, X. Feng, *et al.* Experimental observation of the quantum anomalous Hall effect in a magnetic topological insulator. Science **340**, 167 (2013).
6. Z. F. Wang, Z. Liu, F. Liu. Quantum anomalous Hall effect in 2D organic topological insulators. Physical Review Letters

110, 196801 (2013).

7. X. L. Qi, S. C. Zhang. Topological insulators and superconductors. Reviews of Modern Physics **83**, 1057 (2011).
8. X. Wan, A. M. Turner, A. Vishwanath, *et al*. Topological semimetal and Fermi-arc surface states in the electronic structure of pyrochlore iridates. Physical Review B **83**, 205101 (2011).
9. H. Zhang, J. Wang, G. Xu, *et al*. Topological states in ferromagnetic CdO/EuO superlattices and quantum wells. Physical Review Letters **112**, 096804 (2014).
10. K. Kuroda, T. Tomita, M. T. Suzuki, *et al*. Evidence for magnetic Weyl fermions in a correlated metal. Nature Materials, **16**, 1090-1095 (2017).
11. M. M. Otrokov, I. I. Klimovskikh, H. Bentmann, *et al.* Prediction and observation of an antiferromagnetic topological insulator. Nature (London) **576**, 416 (2019).
12. D. Zhang, M. Shi, T. Zhu, *et al.* Topological axion states in the magnetic insulator $\mathrm{MnBi_2Te_4}$ with the quantized magnetoelectric effect. Physical Review Letter **122**, 206401 (2019).
13. J. Li, Y. Li, S. Du, *et al.* Intrinsic magnetic topological insulators in van der Waals layered $\mathrm{MnBi_2Te_4}$-family materials. Science Advances **5**, eaaw5685 (2019).
14. Y. Deng, Y. Yu, M. Z. Shi, *et al.* Quantum anomalous Hall effect in intrinsic magnetic topological insulator $\mathrm{MnBi_2Te_4}$. Science **367**, 895 (2020).
15. M. M. Otrokov, I. P. Rusinov, M. Blanco-Rey, *et al.* Unique thickness-dependent properties of the van der Waals interlayer antiferromagnet $\mathrm{MnBi_2Te_4}$ films. Physical Review Letter **122**, 107202 (2019).
16. C. Liu, Y. Wang, H. Li, *et al.* Robust axion insulator and Chern insulator phases in a two-dimensional antiferromagnetic topological insulator. Nature Material **19**, 522 (2020).
17. A. Gao, Y.-F. Liu, C. Hu, *et al*. Layer Hall effect in a 2D topological axion antiferromagnet. Nature (London) **595**, 521 (2021).
18. Y.-J Hao, P. Liu, Y. Feng, *et al.* Gapless surface Dirac cone in antiferromagnetic topological insulator $\mathrm{MnBi_2Te_4}$. Physical Review X **9**, 041038 (2019).
19. Y.-J Chen, L.-X Xu, J.-H Li, *et al.* Topological electronic structure and its temperature evolution in antiferromagnetic topological insulator $\mathrm{MnBi_2Te_4}$. Physical Review X **9**, 041040 (2019).
20. Swatek P, Wu Y, Wang L L, *et al*. Gapless Dirac surface states in the antiferromagnetic topological insulator $\mathrm{MnBi_2Te_4}$. Physical Review B **101**, 161109 (2020).
21. Li H, Gao S Y, Duan S F, *et al.* Dirac surface states in intrinsic magnetic topological insulators $\mathrm{EuSn_2As_2}$ and $\mathrm{MnBi_{2n}Te_{3n+1}}$. Physical Review X **9**, 041039 (2019).
22. Hirahara T, Eremeev S V, Shirasawa T, *et al*. Large-gap magnetic topological heterostructure formed by subsurface incorporation of a ferromagnetic layer. Nano letters **17**, 3493 (2017).
23. X. -M Ma, Y. Zhao, K. Zhang, *et al.* Realization of a tunable surface Dirac gap in Sb-doped $\mathrm{MnBi_2Te_4}$. Physical Review B **103**, L121112 (2021).
24. B. Chen, F. Fei, D. Zhang, *et al*. Intrinsic magnetic topological insulator phases in the Sb doped $\mathrm{MnBi_2Te_4}$ bulks and thin flakes. Nature Communication **10**, 4469 (2019).
25. S.-Y. Xu, M. Neupane, C. Liu, *et al.* Hedgehog spin texture and Berry's phase tuning in a magnetic topological insulator, Nature Physics **8**, 616 (2012).
26. S. R. Park, J. Han, C. Kim, *et al.* Physical Review Letter **108**, 046805 (2012).
27. See Supplemental Information at http://link.aps.org/supplemental/10.1103/PhysRevB.103.L121112 for Methods, Sections S1-S15 and Figures S1-S14.

Modulation of Dirac point in magnetic topological insulators $Sn_xMn_{1-x}Bi_2Te_4$

Meng Zeng[a] and Chang Liu[a]

[a] *Department of Physics and Shenzhen Institute for Quantum Science and Engineering (SIQSE), Southern University of Science and Technology (SUSTech), Shenzhen, Guangdong 518055, China*

Keywords: Dirac cone, surface state, magnetic topological insulator, Laser-ARPES

Intrinsic magnetic topological insulators (MTIs), exemplified by $MnBi_2Te_4$, are expected to realize exotic topological quantum phenomena, such as high-temperature quantum anomalous Hall effect (QAHE) and the axion insulator state [1-4]. The realization of QAHE and the axion insulator state requires that the Fermi level be located in the gap of their topological surface states (TSS) [1,2]. Extensive efforts have been made in this field, but there is still a lack of ideal MTI candidates whose energy gap in the TSS is large and at the Fermi energy [5-7]. For the Mn-Bi-Te series, spectroscopic experiments revealed that such a surface gap is much smaller than previously thought. The highly electron-doped nature of the $MnBi_2Te_4$ crystals further obstructs the exhibition of the surface band gap in transport measurements.

Recently, researchers have found that the Fermi level of $Mn(Sb_yBi_{1-y})_2Te_4$ can be tuned from the conduction bands to the valence bands by adjusting the Sb-Bi atomic ratio y [8,9]. Angle resolved photoemission spectroscopy (ARPES) measurement on Sb-doped $MnBi_2Te_4$ revealed a sizable TSS gap, which enlarges along with increasing Sb concentration, enabling simultaneous tunability of the Fermi level and the TSS gap size (up to >100 meV). On the other hand, previous transport studies found an *n-p* transition in $Sn_xPb_{1-x}Bi_2Te_4$ with increasing Sn concentration [10], therefore Sn doping may also represent another route to manipulate the carrier concentration of the Mn-Bi-Te system.

To our best knowledge, no ARPES measurements on $Sn_xMn_{1-x}Bi_2Te_4$ have been reported. In this report, we employed laser ARPES at HiSOR to measure $Sn_xMn_{1-x}Bi_2Te_4$ samples with different doping ratio. We first performed Fermi surface mappings and aligned the Γ point, followed by detailed *k-E* cuts through the surface zone center $\bar{\Gamma}$. As shown in Fig. 1, comparing the Dirac point positions between the pure and Sn-doped samples, we observed that Sn doping acts as hole doping. After doping Sn with $x = 0.1$ and 0.2, the Dirac point have been lifted up for about 40 meV and 53 meV respectively, as compared to the undoped sample, while the gapless Dirac cone remains intact. It is thus expected that on samples with a specific doping concentration, a charge neutral point could be reached, at which the gapless Dirac point located right at Fermi level.

In the future, we anticipate that a magnetic topological system with controllable TSS gap size and a fixed, in-gap Fermi level may be realized in the Sn and Sb co-doped system, $Sn_xMn_{1-x}(Sb_yBi_{1-y})_2Te_4$. Such a system may serve as an ideal platform for the exploration of high-T QAHE as well as its evolution towards the topologically trivial regime.

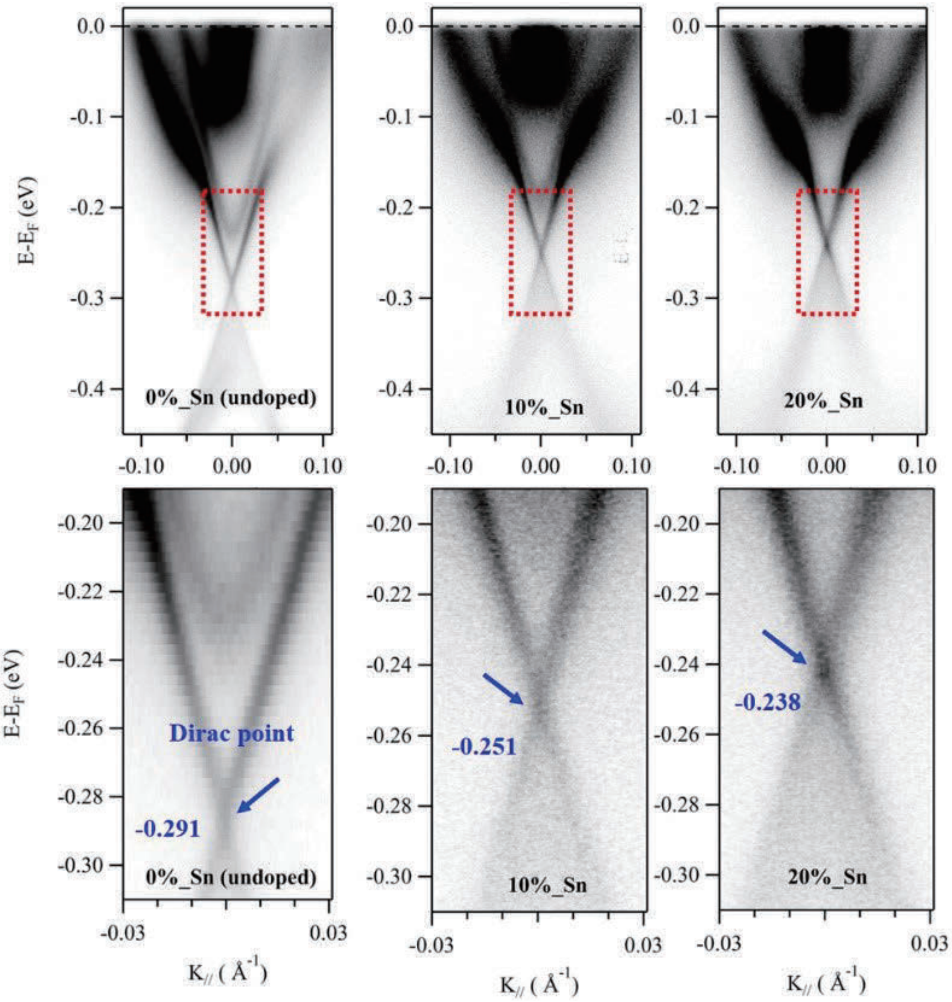

FIGURE 1. The *k-E* cuts at the surface $\bar{\Gamma}$ of $Sn_xMn_{1-x}Bi_2Te_4$ ($x = 0, 0.1, 0.2$) at 10 K. The lifting of Dirac point can be observed clearly.

REFERENCES

1. Y. Deng, Y. Yu, M.-Z Shi, *et al.* Quantum anomalous Hall effect in intrinsic magnetic topological insulator $MnBi_2Te_4$. Science **367**, 895 (2020).
2. C. Liu, Y. Wang, H. Li, *et al*. Robust axion insulator and Chern insulator phases in a two-dimensional antiferromagnetic topological insulator. Nat. mater. **19**, 522 (2020).
3. R. Lu, H. Sun, S. Kumar, *et al.* Half-magnetic topological insulator with magnetization-induced Dirac gap at a selected surface. Physical Review X **11**, 011039 (2021).
4. M.M. Otrokov, I.I. Klimovskikh, H. Bentmann, *et al.* Prediction and observation of an antiferromagnetic topological insulator. Nature **576**, 416 (2019).
5. Y.-J Hao, P. Liu, Y. Feng, *et al.* Gapless surface Dirac cone in antiferromagnetic topological insulator $MnBi_2Te_4$. Physical Review X **9**, 041038 (2019).
6. Y.-J Chen, L.-X Xu, J.-H Li, *et al.* Topological electronic structure and its temperature evolution in antiferromagnetic topological insulator $MnBi_2Te_4$. Physical Review X **9**, 041040 (2019).
7. Y. Hu, L. Xu, M. Shi, *et al*. Universal gapless Dirac cone and tunable topological states in $(MnBi_2Te_4)_m(Bi_2Te_3)_n$ heterostructures. Physical Review B **101**, 161113 (2020).
8. B. Chen, F. Fei, D. Zhang, *et al*. Intrinsic magnetic topological insulator phases in the Sb doped $MnBi_2Te_4$ bulks and thin flakes. Nat. comm. **10**, 4469 (2019).
9. X. -M Ma, Y. Zhao, K. Zhang, *et al.* Realization of a tunable surface Dirac gap in Sb-doped $MnBi_2Te_4$. Physical Review B **103**, L121112 (2021).
10. L. Pan, J. Li, D. Berardan, *et al.* Transport properties of the $SnBi_2Te_4$–$PbBi_2Te_4$ solid solution. Journal of Solid State Chemistry **225**, 168 (2015).

23AU002　23BG039

μ-Laser ARPES

Out-of-plane Spin Texture of Iron-Based Superconductor

Di Wu[a,c] ,Shilong Wu[a,b], Takuma Iwata[d,e], Koji Miyamoto[f], Taichi Okuda[f], Kenta Kuroda[d,e]

[a]Beijing National Laboratory for Condensed Matter Physics,

Institute of Physics, Chinese Academy of Sciences, Beijing 100190, China.

[b]Songshan Lake Materials Laboratory, Dongguan, Guangdong 523808, China.

[c]School of Physical Sciences, University of Chinese Academy of Sciences, Beijing 100049, China.

[d]Graduate School of Advanced Science and Engineering, Hiroshima University,

1-3-1 Kagamiyama, Higashi-Hiroshima 739-8526, Japan.

[e]International Institute for Sustainability with Knotted Chiral Meta Matter (WPI-SKCM2),

Hiroshima University, Higashi-hiroshima 739-8526, Japan.

[f]Research Institute for Synchrotron Radiation Science, Hiroshima University,

2-313 Kagamiyama, Higashi-Hiroshima 739-0046, Japan.

Keywords: Spin-resolved ARPES, Iron-based superconductor.

Extraordinary quantum mechanisms behind the onset of magnetism, nematicity and superconductivity in iron-based superconductors (FeSCs) could be boiled down to the intricate interplay of electronic eigenstates, spin and orbital degrees of freedom combined with certain kinds of symmetry breaking [1-5]. Just like CuO_2 in cuprates and BiS_2 in BiS_2-based family, FeSe/FeAs layer plays an important role in the low energy band structure and behavior. From the symmetry point of view, although the FeSe/FeAs layer has an inversion symmetry center, as is shown in Fig. 1(b), the formation of inversion symmetry would need two Fe sublattices to get involved, each Fe sublattice experiences an opposite crystal field created by out-of-plane Se/As atoms. Therefore, the inversion symmetry of each sublattice would break down locally, which might give a possibility for non-trivial spin textures.

To examine whether the spin texture exist or not, we took bulk FeSe as an example and performed spin-resolved ARPES measurements for the α and β bands near E_F, the measurements of the spin-resolved EDCs were conducted at three momenta positions as shown in Fig. 1(e). The spin-resolved EDCs with red and blue colors clearly distinguish the spin-up and spin-down channels that were derived from the the α and β bands, respectively, where the $E_B(k)$ of the α and β bands located at each momentum position k are represented with the color bars. In contrast with the negligible zero spin polarization of S_Z compounent at point ②, spin polarization of ① and ③ are obvious, as shown in Fig. 1(f), indicating that the spin polarization is mainly along out-of-plane direction of Fermi surface and the maximum value of spin polarization is 40%.

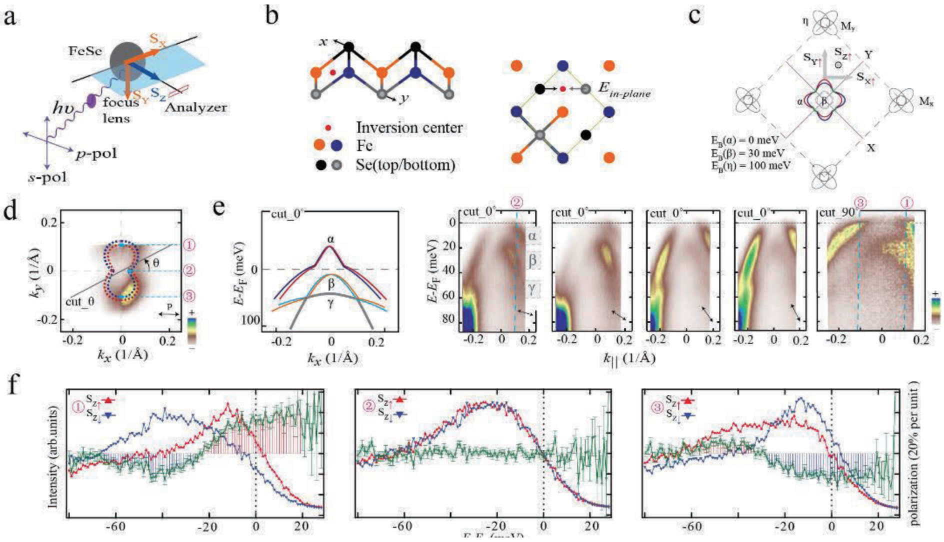

FIGURE 1. Overview of the spin-polarized electronic states with an out-of-plane (z) spin component in bulk FeSe. (a) Experimental configuration of the present micro-sized spin-resolved ARPES measurements. The polarization direction of the incident light is perpendicular (s-polarization) or parallel (p-polarization) to the analyzer slit. The in-plane spin components (Sx and Sy) lie in the ab-plane of FeSe, while the out-of-plane spin component (Sz) is along the c-axis **(b)** Side and top views of the crystal structure of a FeSe single layer with an inversion center connecting two strongly-coupled Fe sublattices **(c)** The calculated Fermi surfaces (FSs) and constant energy contours (CECs) of FeSe in the nematic phase according to our tight-binding models and colored by the non-degenerate spin characters, the effect from twin domains was schematically denoted. **(d)** The experimental FSs of the α bands were measured around Γ point and overlaid with the calculated FSs by the tight-binding model including only a single domain **(e)** Calculated band structures of FeSe and their comparison with the measured results by continuously tuning the light polarization, and the band dispersion along cut rotations (θ=0° or 90°) on the Brillouin zone, where the pink dash lines indicate the momenta positions by performing the spin-resolved EDCs measurements **(f)** Spin-resolved EDCs and their spin polarization. Each panel's encircled number corresponds to the momentum point denoted by the pink dash lines in **(e)**. The green curves present the spin polarization with statistical error bars proportional to $1/\sqrt{N}$, where N is the photoemission intensity.

It is evident that, at the peak positions of the α bands, the spin-down channel at momentum point ① is flipped to the spin-up channel at momentum point ③, the spin flip also occurs at the peak position of the β bands. Such spin flip for the momenta positions ① and ③ reflects, at first glance, the reversal of spin polarization between the α and β bands could be attributed to the orbital-dependent initial states dominated by an effect of the spin-orbital entanglement [6]. In Fig. 1(e), we show the tight-binding model for the tiny band splitting of the α or β bands. However, one could not distinguish the spin splitting of each α or β bands from Fig. 1(f) since the energy resolution of spin apparetus was set to 30 meV. With this in mind that the underlying mechanism for the nematic spin-orbital splitting has remained to be further investigated since both the α and β bands are double-split due to the SOC enhancement or local (ferro)magnetic order in FeSe.

REFERENCES

1. Borisenko, S. V. *et al*. Direct observation of spin-orbit coupling in iron-based superconductors. *Nat. Phys.* **12**, 311-317. (2016).
2. Eugenio, P. M., *et al*. Classification of symmetry derived pairing at the M point in FeSe. *Phys. Rev. B* **98**, 014503. (2018).
3. Li, J. *et al*. Spin-orbital-intertwined nematic state in FeSe. *Phys. Rev. X* **10**, 011034. (2020).
4. Wang, Z., *et al*. Understanding electronic peculiarities in tetragonal FeSe as local structural symmetry breaking. *Phys. Rev. B* **102**, 235121. (2020).
5. Rößler, S., *et al*. Nematic state of the FeSe superconductor. *Phys. Rev. B* **105**, 064505. (2022).
6. Kuroda, K. et al. Coherent control over three-dimensional spin polarization for the spin-orbit coupled surface state of Bi2Se3. *Phys. Rev. B* **94**, 165162. (2016).

23AU003, 23AU009

μ-Laser ARPES
Spin-Laser ARPES

Study Of The Modification Of The Electronic Structure Of $MnBi_2Te_4$ By Doping With Ge Atoms

A.M. Shikin[a] and D.A. Estyunin[a]

[a] *Saint Petersburg State University, 198504 Saint Petersburg, Russia*

Keywords: magnetic dilution, magnetic topological insulators, $MnBi_2Te_4$

The magnetic topological insulator $MnBi_2Te_4$ has garnered significant interest from researchers due to its array of unique electronic properties, such as the quantum anomalous Hall effect and the topological magnetoelectric effect [1-7]. These properties position $MnBi_2Te_4$ as a promising material for applications in spintronics and qubit development. However, controlling the electronic structure and magnetic properties of $MnBi_2Te_4$ remains a significant challenge. One approach to addressing this challenge is magnetic dilution, where Mn atoms are replaced by Ge, Sn, or Pb atoms [8-11]. This substitution alters the electronic structure of $MnBi_2Te_4$ and can induce a topological phase transition. In this work, we investigated the electronic structure of $MnBi_2Te_4$ upon substituting Mn with Ge [$Mn_{1-x}Ge_xBi_2Te_4$)] using laser-based angle-resolved photoemission spectroscopy (ARPES). The study aimed to characterize the topological phase transition and explore the peculiarities of the electronic structure in crystals with compositions close to this transition point.

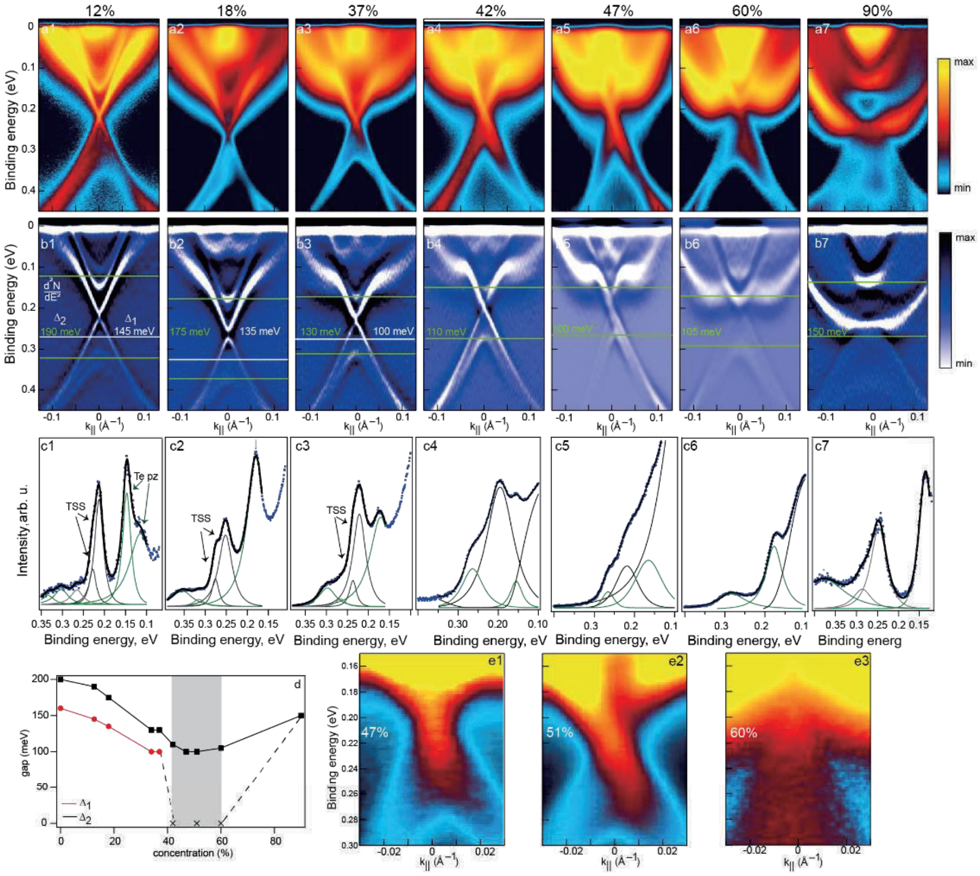

FIGURE 1. Experimental dispersion relations (hν = 6.3 eV) for $Mn_{1-x}Ge_xBi_2Te_4$ (x from 12% to 90%). (a1-a7) - initial spectra N(E,k), (b1-b7) - their second derivative along E, (c1-c7) - decomposition of EDC at the $\bar{\Gamma}$-point. (d) Dependence of the size of the band gap at the $\bar{\Gamma}$-point on x. (e1-e3) Enlarged spectra in the Dirac point region for samples with x from 47% to 60%.

The initial objective was to confirm the presence of topological surface states (TSS) in crystals with varying levels of Mn substitution. To achieve this, measurements were conducted using laser photoexcitation with hv = 6.3 eV. This photon energy is particularly well-suited for resolving TSS in the $MnBi_2Te_4$ family of materials [3, 4–6]. Moreover, laser radiation offers enhanced angular, spatial (spot size 5–10 μm), and energy resolutions (approximately 5 meV).

Figure 1 (a1-a7) presents the experimental dispersion relations of $Mn_{1-x}Ge_xBi_2Te_4$ for a range of Ge concentrations, from 12% to 90%. Figure 1 (a1-a7) illustrates these dispersions as N(E,k), while Figure 1 (b1-b7) shows them as the second derivatives along energy direction (d^2N/dE^2), enhancing the visibility of the observed features. The dispersions are obtained by summing over all measured polarizations (s, p, c+, c−) of the incident laser radiation for panels (a1–a4, a7) and over (s, p)-polarizations for panels (a5, a6). This approach was taken to improve the signal-to-noise ratio, considering the minimal differences in measurement geometries. Figure 1 (c1–c7) displays the corresponding energy distribution curves (EDC) at the $\bar{\Gamma}$-point, which have been decomposed into spectral components to emphasize the TSS and the variations in energy splitting between different states of conduction band (CB) and valence band (VB) as the Ge concentration changes. At lower Ge concentrations, the branches of TSS, along with the nearest states in both the VB and CB, are distinctly visible in the dispersion relations. For instance, in Figure 1 (a1), at a Ge concentration of 12% and a temperature of 16–18 K, the data reveals a splitting of the states in the CB and in the VB, localized at binding energies of 0.10–0.14 eV and 0.31–0.34 eV, respectively. The energy separation between these states in the CB and VB is highlighted by horizontal green lines, denoted as Δ_2. The observed splitting occurs because the spectra were acquired at a temperature below the Néel temperature (i.e. in antiferromagnetic state) for the samples with this specific Ge concentration [3,4,11]. As the Ge concentration increases, the Néel temperature gradually decreases [10]. Consequently, the spectra for samples with higher Ge concentrations were measured only in the paramagnetic state. To compare the variation in the separation between the edges of the CB and the VB at different temperatures, horizontal lines corresponding to Δ_2 were drawn between the midpoints of the observed split states. In Fig. 1(b1-b3) one can observe states near the upper part of the VB at about 0.28 eV. We attribute these states as trivial surface states according to the literature and label them as Δ_1.

Overall, one can see the tendencies of a noticeable decrease in the separation of the VB and CB edges Δ_2 (or Δ_1) with increasing Ge concentration. Quantitatively it is estimated from the decomposition of the EDC and shown in Fig. 1(d) with black and red circles, respectively. The state separations reach average values of about 100 meV in the concentration range of 42-51%, where the separation has a constant value.

It should be noted that the TSS are only clearly visible up to a Ge concentration of approximately 37-42%. However, at a Ge concentration of 47% the TSS are barely distinguishable in the measured data. We expect the appearance of Ge-derived states in the DP region at this concentration. This leads to the formation of a zero-band gap at the $\bar{\Gamma}$-point. These states are visible in Fig. 1(e1-e3). In fact, no clear band gap is observed in these spectra for this range of Ge concentrations. Thus, at these Ge concentrations, the bulk states with the zero gap are formed within the states with a peak energy splitting of about 100 meV (see corresponding EDCs in Fig. 1(c1-c7)). These data also confirm the existence of a zero-band gap plateau at several Ge concentrations, which may indicate the formation of a semimetallic state.

In addition to the described states, the Rashba-like states can be observed in Fig.1 (b1-b6). These states shift towards higher binding energies with increasing Ge concentrations, presumably hybridising with the upper CB and Dirac cone states. This hybridisation leads to the formation of peaks in the EDC profiles with a visible energy splitting of about 100 meV. In the energy region between these peaks, a non-zero density of electronic states is observed, leading to the formation of an apparent zero band gap at the $\bar{\Gamma}$-point.

REFERENCES

1. Y. Tokura, et al., Nature Reviews Physics 1, p. 126, 2019.
2. B.A. Bernevig, et al., Nature 603, p. 41, 2022.
3. M. M. Otrokov, et al., Nature 576, p. 416, 2019.
4. D. A. Estyunin, et al., APL Materials 8, p. 021105, 2020.
5. Y. Hao, et al., Phys. Rev. X 9, p. 041038, 2019.
6. A. M. Shikin, et al., Phys. Rev. B 104, p. 115168, 2021.
7. M. Garnica, et al., Quantum Materials 7, p. 7, 2022.
8. J. Zhu, et al., Phys. Rev. B 103, p. 144407, 2021.
9. T. Qian, et al., Phys. Rev. B 106, p. 045121, 2022.
10. D. A. Estyunin, et al., Magnetochemistry 9, p. 210, 2023.
11. A. S. Frolov, et al., Communications Physics 7, p. 180, 2024.

Current Activities of Research and Education on BL-5 (FY2023)

T. Yokoya[a,b], T. Wakita[a] and Y. Muraoka[a,b]

[a]*Research Institute for Interdisciplinary Science, Okayama University*
[b]*Research Laboratory for Surface Science, Okayama University, Okayama 700-8530, Japan*

Keywords: Photoemission spectroscopy, photoelectron emission microscopy

We present an overview of our resent research and educational activities on beamline 5 (BL5) in the fiscal year 2023. Our beamline has two experimental stations in a tandem way. The first station is equipped with an angle-resolved photoemission spectrometer (ARPES), a low energy electron diffraction (LEED) apparatus and an X-ray source. The hemispherical analyzer of ARPES spectrometer (HA54, VSW) has a mean radius of 50 mm and is mounted on a twin axis goniometer in ultra-high vacuum chamber. Using this goniometer, one can perform ARPES and photoelectron diffraction (PED) measurements. It is also possible to perform resonant photoemission spectroscopy (RPES) measurements by using photon energy tunability of synchrotron radiation with X-ray absorption spectroscopy (XAS) measurement. With the X-ray source (XR2E2, FISONS), we can perform an X-ray photoelectron spectroscopy (XPS) measurement for the chemical state analysis and the PED. At the second station, we have installed a photoelectron emission microscope (PEEM, 'PEEM III', Elmitec). PEEM provides a magnified image of lateral intensity distribution of photo-emitted electrons from a sample surface. The spatial resolutions are several ten nanometers with Hg lamp and a few micrometers with synchrotron radiation. The sample is transferred between the ARPES and the PEEM chamber in-situ, and one can perform measurements at both stations for the same sample.

In the recent researches on BL-5, we have studied the electronic structure of potassium doped aromatic molecule (K_x picene) [1], iron-based superconductor ($FeSe_xTe_{1-x}$) [2], transition metal di-oxide films such as VO_2 thin films which exhibits a first-order metal-to-insulator transition at 340 K [3], CrO_2 thin films which are known as a half-metallic material [4], TaO_2 film which is stabilized with a new technique developed in our group [5], and phase-separated TiO_2-VO_2 films on mica substrates. We have also studied the electronic structures of a high-quality boron-doped diamond film which shows a signature of the highest superconducting transition temperature of 25 K [6] and a high quality single crystal of $YbFe_2O_4$ which is one of multiferroic materials [7], by utilizing RPES at B *K*- and Fe $M_{2,3}$- edges, respectively. In addition, we have studied the sp^3 content in diamond-like carbon films by using photoemission spectroscopy in order to optimize the conditions to produce Q-carbon (quenched carbon) which is a newly discovered amorphous phase of carbon with several exotic properties [8]. In the last few years, we have performed PEEM and TEY measurements at BL5 in HiSOR for (1) a B-doped carbon nano wall film on a Si substrate, (2) a micro-droplet of solidified L-boronophenylalanine (L-BPA) on a Si substrate and (3) cancer cells dosed with L-BPA in order to investigate microscopic chemical states of trace B atoms in them from fine structures in local- and wide-area-XAS spectra near B *K*-edge and to visualize B distributions on their surfaces. For this kind of measurements with PEEM, we have developed a new auto-measurement system where we can obtain a serial PEEM images with excitation x-ray energies for a certain energy range with a fixed energy step.

Recently, we have prepared an auto-measurement system and an X-ray focusing capillary lens for photoemission holography (PEH) measurements. PEH is a method that has been greatly developed in Japan in recent years as a measurement method for elucidating the local structure of materials with an atomic resolution [9]. In particular, various results have been reported in the study of the three-dimensional atomic configurational structure around the dopants in crystals [10]. However, the opportunity to use state-of-the-art apparatuses (for example, DA30 analyzer and RFA of BL25SU at SPring-8) are limited. Although our photoelectron energy analyzer is an old model and it is difficult to separate and observe small shifts in core levels because of the energy resolution of 1-2 eV of the system, we expect that our apparatus will be used for preliminary experiments on undoped materials prior to experiments for doped samples using state-of-the-art systems. It can also be used for educational purposes such as experiencing photoelectron holography experiments and learning the analysis methods.

We have used the BL-5 for education activity as well, for example, practical education for undergraduate students of Okayama University. The students have an opportunity to study the synchrotron radiation mechanism and to experience XPS measurement which is very useful for the surface science research. We accepted more than 100 students from 2006 to 2012. From 2014, we have started to join the practical lecture for experiments using the beamline end stations in HiSOR for both graduate school students of Hiroshima and Okayama Universities. In 2018, we have had a new project for education under a Japan-Asia youth exchange program in science supported by Japan Science and Technology Agency (JST), "Sakura Exchange Program in Science". We have accepted six students from Changchun University of Science and Technology in China.

REFERENCES

1. H. Okazaki *et al*., *Phys. Rev* **82**, pp. 195114 (5 pages) (2010).
2. Y. Yoshida *et al*., *J. Phys. Soc. Jpn* **78**, pp. 034708 (4 pages) (2009).
3. K. Saeki *et al*., *Phys. Rev* **80**, pp. 125406 (5 pages) (2009).
4. Y. Muraoka *et al*., *MRS Proceedings* **1406** (2012).
5. Y. Muraoka *et al*., *Thin Solid Films* **599**, pp. 125-132 (2016).
6. H. Okazaki *et al*., *Appl. Phys. Lett* **106**, pp. 052601 (5 pages) (2015).
7. K. Fujiwara *et al*., *Trans. Mater. Res. Soc. Jpn.* **41**, pp. 139-142 (2016).
8. H. Yoshinaka *et al*., *Carbon.***167**, pp. 504-511 (2020).
9. T. Matsushita *et al*. *Europhys. Lett*. **71**, 597 (2005). *Phys. Status Solidi B* **255**, 1800091 (6 pages) (2018).
10. K. Hayashi, T. Matsushita, *SPring-8 Research Frontiers* **2020**, pp. 12 -15 (2021).

Ex-situ/in-situ Soft X-ray Absorption Investigation on Hydrogen-Induced Corrosion Resistance Degradation of TC4 Titanium Alloy

Hongbo Zhang[a], FeiFei Huang[a*], Hai Chang[a], Hiroaki Yoshida[b] and Ying Jin[a*]

[a]*National Center for Materials Service Safety, University of Science and Technology Beijing, No.30, Xueyuan Road, Haidian District, Beijing P.R. CHINA*
[b]*Department of Physical Science, Hiroshima University, 1-3-1 Kagamiyama, Higashi-Hiroshima, 739-8526, Japan*

Keywords: TC4, titanium alloy, hydrogen charging, oxide film, corrosion resistance, X-ray absorption spectroscopy,

Due to its exceptional properties such as low density, high strength, excellent biocompatibility, super-plasticity, and superior corrosion resistance[1], TC4 (Ti-6Al-4V) titanium alloy is widely used in dental implants[2], biomedicine[3], the marine industry[4], and healthcare products[5]. The excellent corrosion resistance of titanium alloys is primarily due to the formation of a protective oxide film on their surfaces[6]. However, hydrogen-induced damage remains a significant failure mechanism in these alloys[7]. While the mechanical impacts of hydrogen on TC4 have been extensively studied[8], the specific effects of hydrogen on the oxide film's composition, structure, and overall performance are not as well understood. This gap in knowledge highlights the critical need for further research to elucidate how hydrogen influences the protective oxide layer and to develop strategies to mitigate hydrogen-related degradation.

To investigate the impact of environmental hydrogen on the properties and formation mechanism of the oxide film on TC4 titanium alloy, we conducted comprehensive research on its passivation and corrosion resistance. In this study, we specifically examined the effects of hydrogen charging on the formation and dissolution mechanisms of the oxide film on TC4 alloy. Commercial samples of TC4 were subjected to hydrogen charging at a current density of 100 mA/cm^2 in a 3.5% NaCl solution for varying durations (0, 0.5, 1, 4, and 12 hours). Following hydrogen charging, the samples were immersed in the same solution for 5 days to allow stable passivation films to form.

A vacuum sample chamber was designed and installed on BL-6 to reduce the time for changing samples (8-10 samples at once) and enhance the signal-to-noise ratio. Utilizing this chamber, X-ray Absorption Spectroscopy (XAS) was employed to obtain spectra of reference titanium oxides (as shown in Figure 1) and to characterize the complex compositions and chemical states within the oxide film. Additionally, this data supports the findings from X-ray Photoelectron Spectroscopy (XPS), as illustrated in Figure 2. Electrochemical impedance spectroscopy (EIS) was employed using a frequency range of 100 kHz to 10 mHz, at 0 V (vs open circuit potential) with a 10 mV amplitude of the alternating current (AC) signal to research the corrosion resistance of the oxide film. Mott-Schottky measurements were conducted with a potential range from the film-formation potential to -1 V (vs Ag/AgCl reference electrode) at 1000 Hz with a 10 mV amplitude of the AC signal to reveal the semiconductive property of the oxide film. Additionally, polarization curve tests were carried out under conditions referenced to the Ag/AgCl electrode, with a scan rate of 0.33 mV/s and a potential range from -0.5 V to 3 V relative to the open circuit potential.

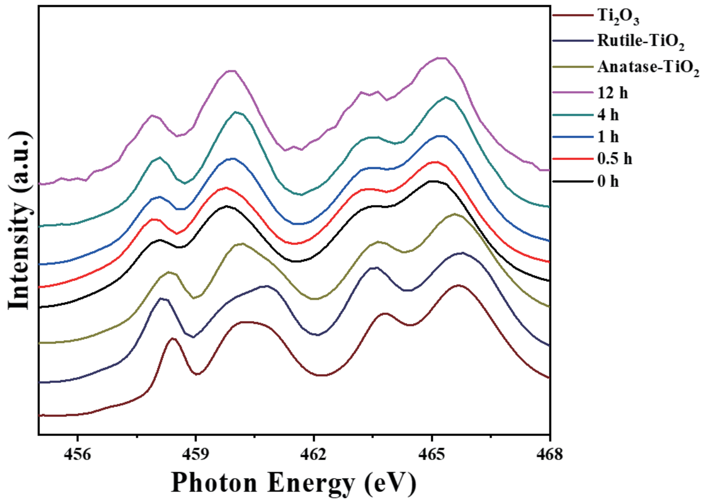

FIGURE 1. XAS spectra (Ti 2p) of reference titanium oxides and the oxide films formed on TC4 alloy after various durations of hydrogen charging.

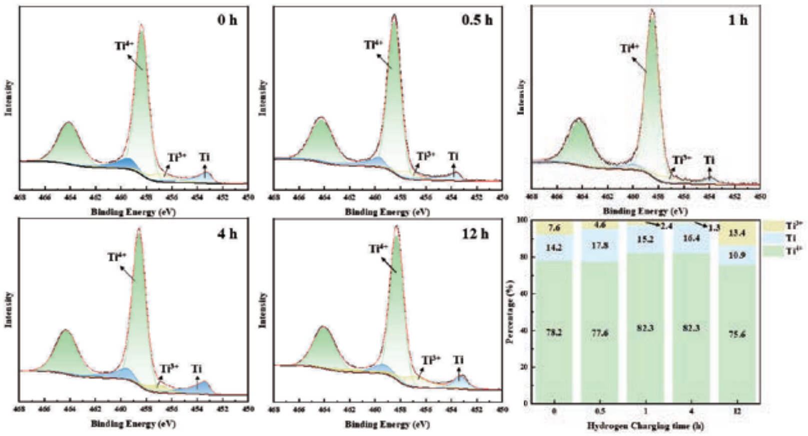

FIGURE 2. High resolution Ti 2p XPS spectra of the oxide films formed on the TC4 alloy after various durations of hydrogen charging.

The main findings are summarized as follows:

(a) The oxide film on the surface of TC4 is primarily composed of TiO_2, with a small amount of Ti_2O_3 also present. Anatase-TiO_2 is more dominant in the oxide film on both hydrogen-charged and non-hydrogen-charged samples.

(b) The content of Ti^{3+} in the oxide film decreases gradually with increasing hydrogen charging time from 0 to 4 hours. However, after 12 hours of hydrogen charging, Ti^{3+} is detected again, which may be related to the hydrogen-induced cracks observed on the surface.

(c) The corrosion resistance of TC4 does not change linearly with hydrogen charging time. Initially, it increases and then decreases with prolonged hydrogen charging. The improvement in corrosion resistance after hydrogen charging is attributed to the densification of the oxide film and the formation of AlOOH. The decrease in corrosion resistance after long-term hydrogen charging is due to the greater stress on the sample surface, leading to hydrogen-induced cracks that reduce the uniformity of the oxide film.

REFERENCES

1. V.A. Alves, R.Q. Reis, I.C.B. Santos, D.G. Souza, T.D.F. Gonçalves, M.A. Pereira-Da-Silva, A. Rossi, L.A. Da Silva, In situ impedance spectroscopy study of the electrochemical corrosion of Ti and Ti–6Al–4V in simulated body fluid at 25 °C and 37 °C, Corros. Sci. 51 (2009) 2473–2482.
2. N. Sakaguchi, M. Niinomi, T. Akahori, J. Takeda, H. Toda, Relationships between tensile deformation behavior and microstructure in Ti-Nb-Ta-Zr system alloys, Mater. Sci. Eng. C. 25 (2005) 363–369. https://doi.org/10.1016/j.msec.2004.12.014.
3. G. He, J. Eckert, Q.L. Dai, M.L. Sui, W. Löser, M. Hagiwara, E. Ma, Nanostructured Ti-based multi-component alloys with potential for biomedical applications, Biomaterials. 24 (2003) 5115–5120. https://doi.org/10.1016/S0142-9612(03)00440-X.
4. C. Lin, Z. Liu, Y. Zhao, Theoretical research on phase transformations in metastable β-titanium alloys, Metall. Mater. Trans. A Phys. Metall. Mater. Sci. 40 (2009) 1049–1058. https://doi.org/10.1007/s11661-009-9798-0.
5. Y.W. Xun, M.J. Tan, Applications of superplastic forming and diffusion bonding to hollow engine blades, J. Mater. Process. Technol. 99 (2000) 80–85. https://doi.org/10.1016/S0924-0136(99)00377-5.
6. T.B. Kim, W.H. Jung, H.S. Ryu, K.W. Kim, J.H. Ahn, K.K. Cho, G.B. Cho, T.H. Nam, I.S. Ahn, H.J. Ahn, Electrochemical characteristics of Na/FeS2 battery by mechanical alloying, J. Alloys Compd. 449 (2008) 304–307. https://doi.org/10.1016/j.jallcom.2006.02.113.
7. M. Niinomi, Recent research and development in titanium alloys for biomedical applications and healthcare goods, Sci. Technol. Adv. Mater. 4 (2003) 445–454.
8. Perini N, Corradini P G, Nascimento V P, et al. Characterization of AISI 1005 corrosion films grown under cyclic voltammetry of low sulfide ion concentrations[J]. Corrosion Science, 2013, 74(Complete):214-222.

23BU005 BL-6

Molecular orientation in polymer/fullerene blend films studied by NEXAFS

Y. Hanaki[a], H. Yoshida[b,c] and T. Sekitani[b,c]

[a]Faculty of Science, Hiroshima University
[b]Graduate School of Advanced Science and Engineering, Hiroshima University
[c]Hiroshima Synchrotron Radiation Center, Hiroshima University

Keywords: fullerene, polymer, solar cell, NEXAFS

With the increasing demand for renewable energy, organic photovoltaics have attracted much attention due to the low cost, lightweight and flexibility in recent years. Polymer solar cells based on bulk heterojunction (BHJ) consisting of interpenetrating networks of conjugated polymers as electron donors and fullerene derivatives as electron acceptors, are being developed for their potential application [1]. They provide a large interfacial area where efficient exciton dissociation can occur. The morphology of BHJ plays an important role in obtaining high efficiency organic photovoltaic devices. The order and orientation of the polymer backbone in the bulk heterojunction can influence device properties, such as the exciton diffusion, and charge carrier transport.

In this study, the molecular orientation of polymer/fullerene blend film was examined by near edge X-ray absorption fine structure (NEXAFS) spectroscopy. Poly-{bi(dodecyl)thiophene-thieno[3,4-c]pyrrole-4,6-dione} (PBTTPD) was used as electron donor, and (6,6)-phenyl-C_{61}-butyric acid methyl ester (PCBM) is used as electron acceptor. Figure 1 show the molecular structures of PBTTPD and PCBM. The blend of poly-3-hexylthiophene (P3HT) and PCBM has been used as a model system in BHJ solar cells. Compared with P3HT, PBTTPD is co-polymer which has donor and acceptor in the main chain and the higher power conversion efficiency of PBTTPD blend film is reported [2].

Samples for NEXAFS measurement were spin-coated on the gold coated silicon substrate from each solution. Pure PBTTPD PCBM, and blend of PBTTPD:PCBM (1:1.5 by weight) were dissolved in chloroform. NEXAFS measurements were performed at BL6 of Hiroshima Synchrotron Radiation Center.

Oxygen K-edge NEXAFS spectra were measured for PBTTPD, PCBM and PBTTPD: PCBM blend films. Figure 2 shows the NEXAFS spectra of blend films. Red line shows spectrum of normal incidence and black line shows that of grazing incidence. First strong peak come from $\pi^*_{C=O}$ resonant excitations of both PBTTPD and PCBM. NEXAFS spectrum of blend film was well reproduced by the superposition of PBTTPD and PCBM. From the angular dependence of $\pi^*_{C=O}$ excitation, orientation angle of each molecule was obtained. Both PBTTPD of pure and blend films show "edge-on" orientation, which has the plane of polymer backbone perpendicular to the substrate. The effect of the coexistence of PCBM is considered small for polymer orientation which is important for charge transport process.

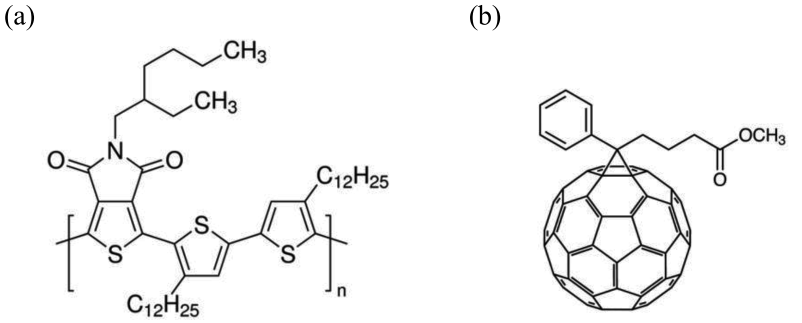

FIGURE 1. Molecular structures of (a) PBTTPD and (b) PCBM.

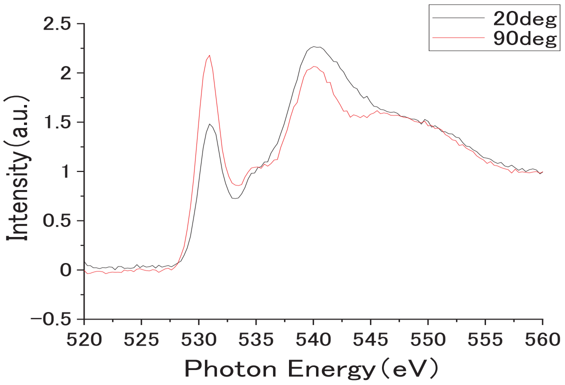

FIGURE 2. Oxygen K-edge NEXAFS spectra of PBTTPD:PCBM blend film measured at different incidence angle.

REFERENCES

1. G. Yu, J. Gao, J. C. Hummulen, F. Wudl, A.J. Heeger, *Science* **270**, 1789 (1995).
2. M. S. Su, C. Y. Kuo, M. C. Yuan, U. S. Jeng,; C. J. Su, K.-H. Wei, *Adv. Mater.* **23**, 3315 (2011)

Electronic Density of States of Selenium Chain within Single Walled Carbon Nanotube

H. Ikemoto[a], K. Mimura[b], R. Nishikawa[a], and H. Sato[c]

[a]Faculty of Science, University of Toyama, Toyama 930-8555, Japan
[b]Graduate School of Engnr., Osaka Metropolitan University, Osaka 599-8531, Japan
[c]Hiroshima Synchrotron Radiation Center, Hiroshima University, Higashi-Hiroshima 739-0046, Japan

Keywords: chalcogen chain, carbon nanotube, electronic density of states.

Chalcogen elements are unique in that they have a hierarchical structure. The coexistence of the strong covalent bonds and the weak inter-chain interactions, which is due to the overlap between lone pair (LP) and antibonding (σ*) orbitals on adjacent chains, leads to interesting structures and properties. When the atoms are confined in the narrow one-dimensional channel, they form chains with two-fold covalent bond because of the strong covalent bond and the weak interchain interaction. Carbon nanotube (CNT) has an ideal space for the synthesis of these chains due to its size of about 10 Å diameter and weak interaction with the chalcogen elements. We study the physical properties of selenium chains based on the electronic density of states (EDOS) observed by photoemission spectroscopy (PES).

Se chains confined in SWCNT (Se@SWCNT) was fabricated by heat treatment, that is, Se bulk and single-walled CNT (SWCNT) were sealed in a glass tube and heated to 973 K for 48 hours [1]. The insertion of Se atoms into SWCNT was confirmed by electron microscopy. PES measurements were performed using high-resolution PES spectrometer installed at BL-7 of HiSOR in the incident photon energy range ($h\nu$) of 60-450 eV at room temperature (RT). The measurements for valence band EDOS were performed in the incident photon energy range of 60-120 eV, and those for core-level PES spectra for the C 1*s*, Se 3*d* levels to examine the chemical states around each element. The binding energy was calibrated to 4*f* level and the Fermi edge of Au film.

Figure 1 shows the valence band spectra for trigonal Se (t-Se), SWCNT and Se@SWCNT, respectively, where background was subtracted using LG4X [2] and the spectra were normalized to the highest peak. In the spectra for t-Se, the peaks around 2.6, 5.6 and 14 eV were assigned to the lone pair (LP), bonding (σ) and s orbitals respectively. Band gap was observed, indicating that t-Se is semiconductor. In SWCNT there were peaks at 3.1, 5.8, and 15 eV. The spectra of Se@SWCNT were quite similar to those of SWCNT above 8 eV. This is natural because Se atoms were inserted into the SWCNT and most of the photoelectron signals came from SWCNT.

To obtain the spectra of the Se chains encapsulated in SWCNT, the spectra of Se@SWCNT were substituted by those of SWCNT. In this procedure the spectra were normalized to the peak at 7.5 eV, since the peak was highest and only appeared for SWCNT. The subtracted spectra are shown in Figure 2. At RT the band gap became larger than that of t-Se. In t-Se the overlap between LP and σ* orbitals on adjacent chains weakens the covalent bond. When Se chains were isolated in SWCNT, the overlap disappeared. Therefore, the covalent bond was strengthened in SWCNT, resulting in widening of the band gap. In contrast to Se@SWCNT at RT, the band gap closed at 20 K. According to our extended X-ray absorption fine structure analysis, the coordination number of the covalent bond decreased from 2.0 to 1.8 with decreasing temperature. These results suggest that a transition occurred, but understanding this phenomenon requires further study including *ab initio* calculations.

The authors appreciate Dr. Fujimori for providing the sample.

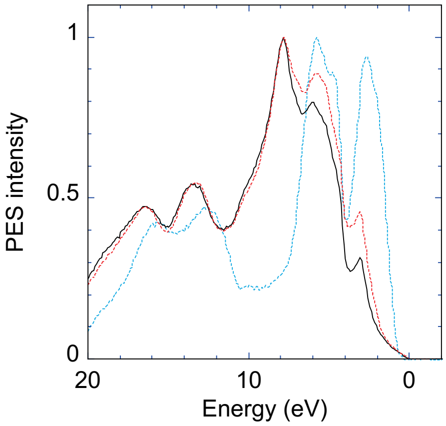

FIGURE 1. PES spectra of t-Se (blue), SWCNT (black), and Se@SWCNT (red) at RT.

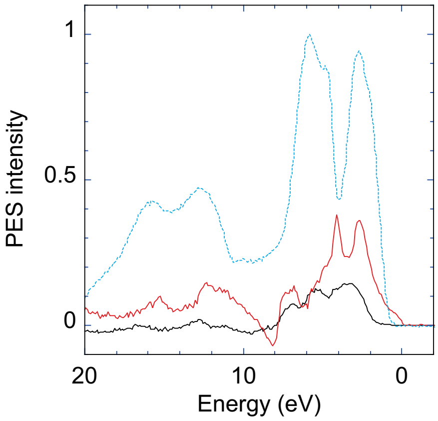

FIGURE 2. PES spectra of t-Se (blue), the difference between Se@SWCNT and SWCNT at RT (black), and at 20K (red).

REFERENCES

1. T. Fujimori, et al., Nature Communication, **4** (2013) 2162.
2. LG4X; https://github.com/hidecode221b/LG4X

Fe 3*d* electronic State in Covalent Chain Antiferromagnets $TlFeX_2$ (X = S, Se) Investigated by Resonant Photoemission Spectroscopy

K. Mimura[a], T. Shinozuka[a], K. Shimooka[a], Y.-G. Shim[a], K. Wakita[b],
Z. Jahangirli[c], I. Amiraslanov[c], H. Sato[d], and N. Mamedov[c,e]

[a] *Department of Physics and Electronics, Osaka Metropolitan University, Sakai 599-8531, Japan*
[b] *Faculty of Engineering, Chiba Institute of Technology, Narashino, Chiba 275-0016, Japan*
[c] *Institute of Physics, Azerbaijan National Academy of Science, Baku 1143, Azerbaijan*
[d] *Hiroshima Synchrotron Radiation Center, Hiroshima University, Higashi-Hiroshima, Japan*
[e] *Institute of Physical Problems, Baku State University, Baku Az1148, Azerbaijan*

Keywords: Covalent chain antiferromagnet, Electronic structure (Fe 3*d* state), Resonant photoemission spectroscopy.

The covalent chain antiferromagnets $TlFeX_2$ (X = S, Se) have attracted much interest because of their quasi-one-dimensional magnetic properties due to the larger intrachain super-exchange interaction compared to the interchain direction [1]. $TlFeS_2$ and $TlFeSe_2$ exhibit antiferromagnetism, which the spins are anti-parallel and aligned anti-parallel in the direction perpendicular to the chain, below Néel temperatures of 196 K and 290 K, respectively [2]. The magnetic properties of this system are mainly determined from the Fe 3*d* electronic state, but no direct observation of the electronic state has been reported. In this study, we have investigated the electronic structure by means of Fe 3*p*-3*d* resonant photoemission spectroscopy (RPES) so as to discuss the Fe 3*d* electronic state in $TlFeX_2$.

Samples used were $TlFeX_2$ single crystals grown by the Bridgman method. The Fe 3*p*-3*d* RPES measurements were performed at BL-7, HiSOR. Overall energy resolution was estimated to be 65 meV from the spectrum of the Fermi edge of Au film. All the spectra were collected at the room temperature.

Figure 1 shows the photon energy (*hν*) dependence of RPES spectra for $TlFeX_2$ observed in the Fe 3*p*-3*d* absorption region. Intensities are normalized to the monochromator output. One notices that four structures labeled from 1 to 4 exhibits prominent resonance. With increasing *hν* from 50 to 70 eV, the intensities of these structures decrease until the minimum at *hν* = 54 eV (off-resonance) and reach the maximum at *hν* = 57 eV (on-resonance).

The off-resonance spectra of both $TlFeX_2$ are well in agreement with self-consistent band structure calculations based on the full-potential linearized augmented plane wave (FLAPW) method [3]. According to the FLAPW band, the off-resonance spectrum of $TlFeS_2$ ($TlFeSe_2$) is mainly composed from Tl 6*s* and S 3*p* (Tl 6*s* and Se 4*p*).

The strong influence of Fe MMM Auger and Tl OOO Auger (due to secondary light) components in the valence band spectra makes it very difficult to extract the Fe 3*d* partial density of states from the RPES spectra. For $TlFeSe_2$, especially, the Se 3*d* core levels excited due to secondary light overlap the valence band RPES spectrum. However, we can discuss the hybridization strength between Fe 3*d* and the conduction electrons from the structures near the valence band maximum in the on-resonance spectrum. The intensity of structure 1 to structure 2 for $TlFeS_2$ is larger than that for $TlFeSe_2$, suggesting that the hybridization strength between Fe 3*d* and the conduction electrons is stronger in $TlFeS_2$. This result is consistent with the results obtained from the valence band and Fe 2*p* HAXPES spectra [3].

REFERENCES

1. E. B. Asgerov, N. T. Dang, D. I. Ismayilov, S. E. Kichanov, R. N. Mechdiyeva, A. I. Madadzada, S. H. Jabarov, E. M. Kerimova, and E. V. Lukin, *Mod. Phys. Lett. B* **29**, 1550024 (2015).
2. Z. Seidov, H. A. Krug von Nidda, J. Hemberger, A. Loidl, G. Sultanov, E. Kerimova, and A. Panfilov, *Phys. Rev. B* **65**,

014433 (2001).

3. K. Mimura, S. Motonami, Y.-G. Shim, K. Wakita, Z. Jahangirli, O. Alekperov, N. Mamedov, H. Sato, Y. Utsumi, S. Ueda, K. Shimada, Y. Taguchi, K. Kobayashi, G. Bihlmayer, H. Namatame, and M. Taniguchi, *Phys. Status Solidi C* **10**, 989-992 (2013).

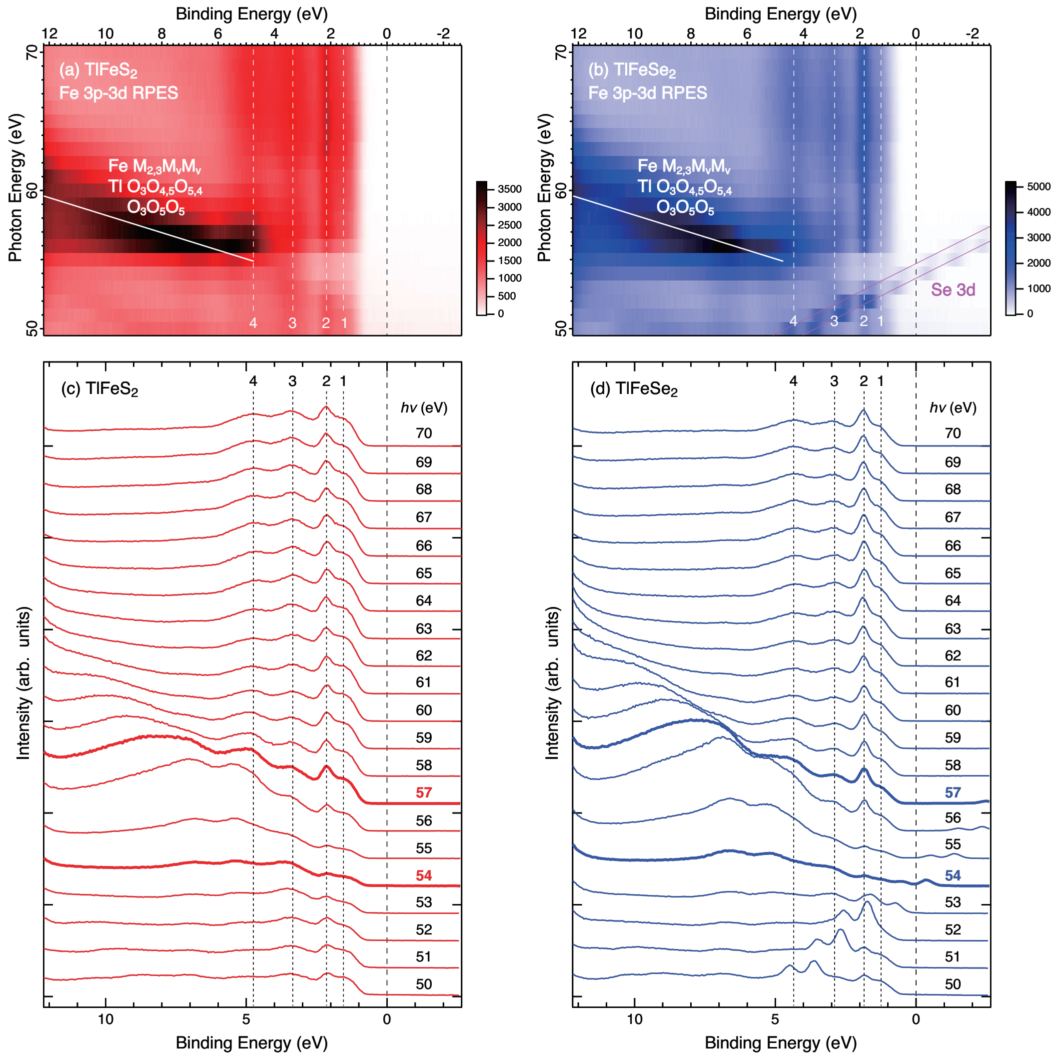

FIGURE 1. Photon energy (*hv*) dependence of RPES spectra for TlFeX$_2$. (a), (b) Image plot of X = S and Se, respectively. (c), (d) *hv* dependence of EDC plot of X = S and Se, respectively. Labels 1 to 4 indicate the binding energy position at which the constant initial state (CIS) spectra were extracted.

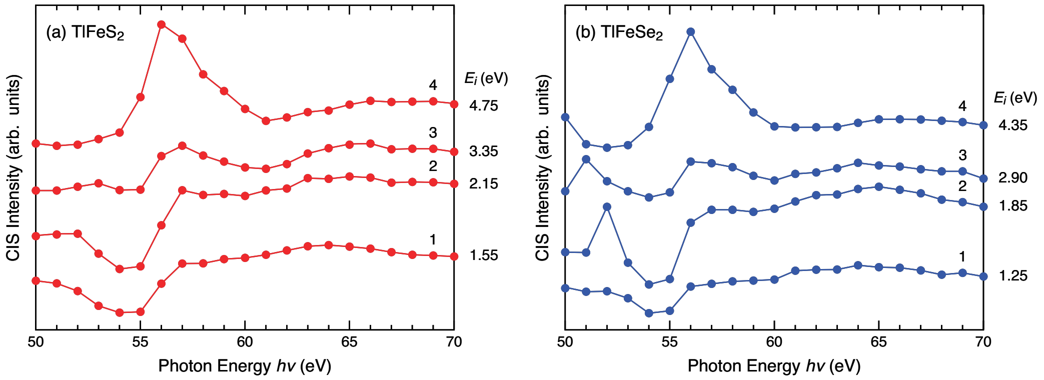

FIGURE 2. Initial (binding) energy E_i dependence of the CIS spectra for TlFeX$_2$. (a) X = S. (b) X = Se.